Use of a Radar Simulator on the Output Fields from a Numerical Mesoscale Model to Analyze X-Band Rain Estimators

E.-P. Zahiri, M. Gosset, J.-P. Lafore, V. Gouget

Use of a Radar Simulator on the Output Fields from a Numerical Mesoscale Model to Analyze X-Band Rain Estimators

E.-P. ZAHIRI AND M. GOSSET

Institut de Recherche pour le Développement, Laboratoire d'étude des Transferts en Hydrologie et Environnement, Grenoble, France

J.-P. LAFORE AND V. GOUGET

Centre Nationale de Recherches Météorologiques, Toulouse, France

ABSTRACT

A full radar simulator, which works with the 3D output fields from a numerical mesoscale model, has been developed. This simulator uses a T-matrix code to calculate synthetic radar measurements, accounts for both backscattering and propagation effects, and includes polarimetric variables. The tool is modular to allow several options in the derivation of the synthetic radar variables. A measurement uncertainty can be taken into account on both the simulated reflectivities and the differential phase shift. A scheme can also be switched on to allow for the gate-to-gate variability of the rain drops size distribution or, also, their oblateness. This work was done in the framework of the installation in West Africa of a polarimetric X-band radar for the observation of tropical rain. Accordingly, the first objective pursued with this simulation setup is a detailed analysis of X-band polarimetric rain retrieval algorithms. Two retrieval schemes, a simple R–K_{DP} formula and a profiler that uses both reflectivity and ϕ_{DP}, are tested. For that purpose the simulator is run on a model case study of an African squall line, then the two schemes are used to retrieve the rain rates from the synthetic radar variables and compare them to the original. The scores of the schemes are discussed and compared. The authors analyze the sensitivity of the results to the measurement uncertainty and also to several aspects of drop size distribution and drop shape variability.

1. Introduction

Numerical simulation of weather radar observations raises the interest of the community for two main reasons: first of all, realistic simulations are convenient for carrying out detailed sensitivity analyses. With a numerical tool it is easy to analyze independently the different sources of error and uncertainties affecting radar measurements and retrieval algorithms (Zawadzki 1984; Testud et al. 2000). Focusing only on works that were concerned with rain estimation, we can give a few examples of such simulation-based sensitivity analysis. Fabry et al. (1992) analyzed the influence of radar resolution and range on rain estimation. Sánchez-Diezma et al. (2000) presented a detailed study, based on simulation, of the visibility of the bright band, according to the characteristics of volumetric scans. Ryzhkov and Zrnić

(1998) and Gosset (2004) tackled the problem of nonuniform beam filling (NUBF) of the radar beam and its effect on the differential phase shift. Gosset and Zawadzki (2001) and Berne and Uijlenhoet (2005) focused on the problem of drop size distribution variability and NUBF on attenuation correction techniques. We could also cite the work by Pellarin et al. (2002), who simulated the interception of the radar beam by ground targets to analyze its effect on rain estimates in mountainous regions. The second and more recent source of interest for radar simulators is linked to the prospect of radar data assimilation in prediction models (Caumont et al. 2005; Wu et al. 2000; Xiao et al. 2004). For that purpose radar operators need to be coded within the meteorological models. Caumont et al. (2005) and Haase and Crewell (2000) presented full radar simulators that they developed within high-resolution nonhydrostatic models and compared with real radar observations for validation purposes.

The simulation setup introduced in the present paper was developed primarily for the analysis of radar rain

Corresponding author address: Marielle Gosset, I.R.D.–Cotonou, 08 B.P. 841, Aéroport, Bénin.
E-mail: marielle.gosset@ird.fr

341

estimators rather than for data assimilation purposes. However, the simulator is applied to rain fields generated by a mesoscale model. The idea is to take advantage of the richness of a high-resolution mesoscale model output and use it as a numerical data bank to carry out various sensitivity studies. The simulator presented here mimics radar scans inside the three-dimensional high-resolution fields issued from the model. Afterward, rain retrieval algorithms are applied to this synthetic radar data and the estimated rain fields compared to the original ones.

The present work was carried out as part of the preparation of a big field campaign: the African Monsoon Multidisciplinary Analysis (AMMA; Redelsperger et al. 2006) project. This international program and field campaign aims at a better understanding of the African monsoon system, its variability, and its impact on the water resources in West Africa. As part of this experiment a variety of hydrological and meteorological instruments have been and will be deployed in several West African countries (Redelsperger et al. 2006; additional information is available online at http://amma-international.org), to document the physical processes and quantify the different terms of the water budget over a range of scales. As part of the three-years-long enhanced observing period (EOP) an X-band polarimetric radar, Xport (Cazenave et al. 2006), has been set up by the Institut de Recherche pour le Développement (IRD) in northern Benin to monitor and estimate rainfall over a small, well-instrumented watershed. The primary aim of our simulator and of the study presented in this paper is to anticipate the behavior of such an X-band radar in typical African rainfall. We also wanted to carry out detailed sensitivity analysis on several rain retrieval algorithms planned to be used on our polarimetric X-band radar.

Several authors have proposed in the recent years the use of X-band radar for rain estimation (Sauvageot 1996; Matrosov et al. 1999, 2002, 2005; Testud et al. 2000; Anagnostou et al. 2004; Park et al. 2005a,b). In circumstances where long-range coverage is not essential, such radar offers the advantages of lower cost, compactness, and transportability over traditional S- or C-band systems. The renewed interest for X-band radar is mainly due to polarimetric techniques that offer new ways to overcome the problem of partial attenuation by rain. Several methods have been proposed to do so. Sauvageot (1996) presented a method based on the measurement of the differential reflectivity Z_{DR} and an iterative estimation of the differential attenuation A_{DP} to estimate the rain rate. Other authors (Matrosov et al. 1999, 2002, 2005; Testud et al. 2000; Anagnostou et al. 2004; Park et al. 2005a,b) exploited the quasi-linear re-

lation that exists between the differential phase shift and the path-integrated attenuation. A few experiments have confirmed the potential usefulness of these approaches (Matrosov et al. 2005; Park et al. 2005b; Anagnostou et al. 2004). However, as the proposed techniques and instrument are new, the experimental tests are limited to a few case studies and the ground validation is too limited to have a robust evaluation of the performance. The cited authors, on the other hand, have made an effort to test their algorithms using simulations. However, these individual studies tend to have different starting assumptions and also tend to focus on one specific aspect of the problem. This makes it difficult to compare their results. In Sauvageot (1996), for instance, the coefficients of the relationships between the various radar parameters and between differential reflectivity and rain are fixed, and the scheme is supposed to correct mainly for miscalibration. Matrosov et al. (2005), following Gorgucci et al. (2000, 2001), interpreted the variability between the radar polarimetric variables as an indication of changes in the aspect ratio of the drops within the storm. The method proposed by Testud et al. (2000) interprets the variability in term of changes in one parameter of the drop size distribution (DSD): the normalized intercept parameter N_0. It should be noted that none of these studies, including the very comprehensive one by Testud et al. (2000), consider the stochastic aspect of DSD variability.

This paper examines the various terms that influence the X-band polarimetric rain estimators and compares their weight in the final result. For this, we compare at the same time and with the same simulation setup several sources of uncertainties, which are (i) the natural variability of the drop size distribution both from storm to storm and within a storm, (ii) the shape of drops and its variability, (iii) the temperature of the medium, (iv) the range of rain rates and their distribution within the storm, and (v) measurement uncertainties.

Because of the targeted application, we focus on a warm tropical environment with medium to heavy rainfall rates. Also, we deal only with rain estimators that use the differential phase shift ϕ_{DP} or its derivative K_{DP}, and we focus on the X-band, which is the operating frequency of our radar. To achieve the objectives above, the radar simulator uses as input fields, those generated by the mesoscale model Meso-NH (Lafore et al. 1998) run for a case study of a West African squall line.

Section 2 describes the radar simulator and explains how it uses the output from the model. Section 3 presents several X-band rain estimators and analyses the variability of the polarimetric radar variables and of
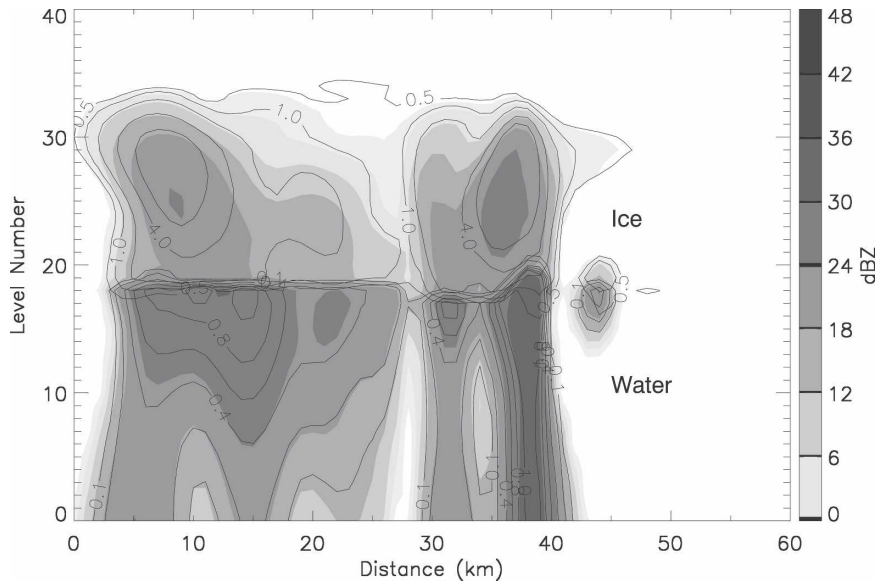
FIG. 1. Example of a vertical slice in an African squall line generated by Meso-NH. The numbers on the contours indicate hydrometeor mixing ratios, used as an input for the radar simulator. The shaded areas represent the reflectivity factors (dBZ) calculated by the model. The y axis indicates the vertical level number in the model. The separation between solid (above around level 18) and liquid hydrometeors is visible, on both the reflectivity and mixing ratio contours.

their relationship to rain. In section 4, we use the simulation setup to quantify the effect of these various uncertainties on the skills of the two selected retrieval schemes. The scores of the retrieval schemes are compared and the results also analyzed as a function of the range of rain rates considered. We close the discussion and present our perspectives in section 5.

2. Simulation setup

This section presents the various steps and modules used to produce the synthetic radar data from the mesoscale model output fields. The core of the radar simulator is a T-matrix code (Mishchenko and Travis 1998), which is used to calculate the scattering properties of individual drops modeled as oblate spheroids. Then, for each radar gate, the scheme performs the integration over the DSD. Finally, the propagation parameters are integrated in range and a measurement uncertainty can be added to output the synthetic radar "measurements." The details of the whole scheme are given below (and summarized in the diagram in Fig. 4).

a. Step 1: From model's mixing ratios to DSDs and radar intrinsic variables

The model output fields of interest for us are the mixing ratios (Fig. 1). In the model version we use,

three types of frozen hydrometeors (ice, snow, and graupel) and two types of liquid hydrometeors (cloud water and rain) are represented. The results presented in this paper are only for low-elevation scans in a warm environment, so that only the mixing ratio for rain is useful. These variables are provided on the three-dimensional Cartesian grid of the model. Once the position of the radar in that grid is set, the interpolation scheme developed at Météo-France by Caumont et al. (2005) is used to provide us with data on a polar grid, with the following coordinates: the distance to the radar, the elevation, and the azimuth angles. Unlike in Caumont et al. (2005), our radar simulator is totally external to the mesoscale model. This offers more flexibility, and allows us to add, for instance, a random variability to the drop size distribution, as will be explained below. Once the model data of interest (i.e., the mixing ratios and air density) are extracted, they are converted into a water content profile along each radial. The next step is to associate a drop size distribution at each radar range gate. To derive a DSD from the liquid water content (LWC) several assumptions need to be made. In the Meso-NH model microphysics scheme, for instance, the DSD is exponential with the intercept parameter set by default to the Marshal–Palmer value (8000 m^{-3} mm^{-1}). For our radar simulations, however, we chose to have more flexibility and we adopt three-parameter normalized gamma distribu-

tions (Testud et al. 2001; Illingworth and Blackman 2002):

$$n(D) = N_0 \frac{\Gamma(4)(3.67 + \mu)^{4+\mu}}{3.67^4 \Gamma(4 + \mu)} \left(\frac{D}{D_0}\right)^\mu \exp\left[-\frac{(3.67 + \mu)}{D_0} D\right],$$

$$(1)$$

with $n(D)$ $(mm^{-1}m^{-3})$, D in mm, D_0 is the median volumetric diameter, μ the shape parameter of the DSD, and N_0 $(mm^{-1}m^{-3})$ is a characteristic number, equal to the intercept parameter of the exponential DSD ($\mu = 0$) having the same water content. Here N_0 is expressed at each gate as a function of the water content:

$$N_0 = \frac{10^9 6(LWC)3.67^4}{\rho_w \pi \Gamma(4) D_0^4},$$

$$(2)$$

with the water content LWC (kg m^{-3}) and the density of water ρ_w (kg m^{-3}).

The DSD is derived at each radar gate, from the LWC, using Eqs. (1) and (2) and assumptions have to be made about the values of N_0 and μ. We keep, as our reference configuration, μ equals 0 and N_0 set to 8000 m^{-3}mm^{-1}, but we can also impose a different value of N_0, either for the entire simulation or by imposing a gate-to-gate variability of N_0 as illustrated in Fig. 2 and further discussed in section 4. Once the DSD is set, the radar intrinsic parameters at each gate are calculated, by integrating over the DSD, the individual scattering functions (see, e.g., Bringi and Chandrasekar 2001, for the definition of the scattering functions and the calculations of the radar variables) calculated with a T-matrix code (Mishchenko and Travis 1998). By intrinsic parameters we mean the reflectivity factors for both horizontal and vertical polarization, both specific attenuations A_H and A_V, the specific differential phase shift K_{DP}, and the phase shift on backscattering, δ. It is noteworthy that at this stage the minimum and maximum diameters (D_{min} and D_{max}) over which the integration is performed, can be adjusted, for instance to study the effects of truncation or conversely of "big drops" (Carey et al. 2000). The default values are from 0.1 to 5 mm in 0.1 mm steps.

An example of the range profiles of water content, DSD parameters, and intrinsic variables is illustrated in Figs. 2 and 3.

b. Step 2: From radar intrinsic variables to synthetic measurements

At this stage, the propagation parameters (specific attenuation and specific phase shift) are integrated

along the path to calculate the attenuated reflectivities and differential phase shift at range r. The equation in dBZ is

$$Z_{im}(r)_{dBZ} = Z_i(r)_{dBZ} - 2 \int_0^r A_i(s) \, ds,$$

$$(3)$$

with $I = H$ or V indicates the polarization, and $A_{H,V}$ is in dB km^{-1}.

The differential phase shift at each gate is calculated by

$$\phi_{DP}(r) = 2 \int_0^r K_{DP}(s) \, ds + \delta(r);$$

$$(4)$$

ϕ_{DP} is in degrees, K_{DP} is the specific differential phase shift ($^\circ$ km^{-1}), and δ the differential phase shift on backscattering ($^\circ$).

To take into account a realistic radar coverage, a radar minimum detectable reflectivity (MDR)—below which the reflectivity is ignored—is also chosen, according to the characteristics of the radar to be simulated.

At this stage a measurement uncertainty can be taken into account, both on the reflectivity and on the phase shift.

For the reflectivity, the uncertainty is modeled as an additive (dBZ) random error ε_Z. This error is normally distributed (Gaussian) over the entire scan and uncorrelated from gate to gate or from radial to radial (in practice this is implemented in the code with a random generator that uses the Box–Muller method). The standard deviation of ε_Z, σ_{ε_Z}, is chosen by the user. We usually set it to 1 dBZ, which is the classical value found in the literature for standard radar characteristics and postprocessing. Profiles of intrinsic reflectivity (Z_H) and the corresponding "measured" reflectivity with an uncertainty σ_{ε_Z} of 1 dBZ, are presented in Figs. 3a,c.

For the phase shift ϕ_{DP} the uncertainty function is also additive. It is constructed to take into account the degradation of the phase signal when the signal-to-noise ratio (SNR) decreases. When the SNR is high (in practice for Z_{Hm}-MDR above a given threshold), the error is normal with a standard deviation $\sigma_{\varepsilon_\phi}$. When Z_{Hm} is low compared to the MDR, the differential phase signal should be dominated by the one of noise and be uniformly distributed over $(-\pi, \pi)$. This is done by adopting the following equation:

$$\phi_{DPm} = [\phi_{DP} + \varepsilon_\phi f(SNR)] \, MOD \, \pi,$$

$$(5)$$

with ε_ϕ a normally distributed variable with standard deviation $\sigma_{\varepsilon_\phi}$. The function $f(SNR)$ is equal to 1 when
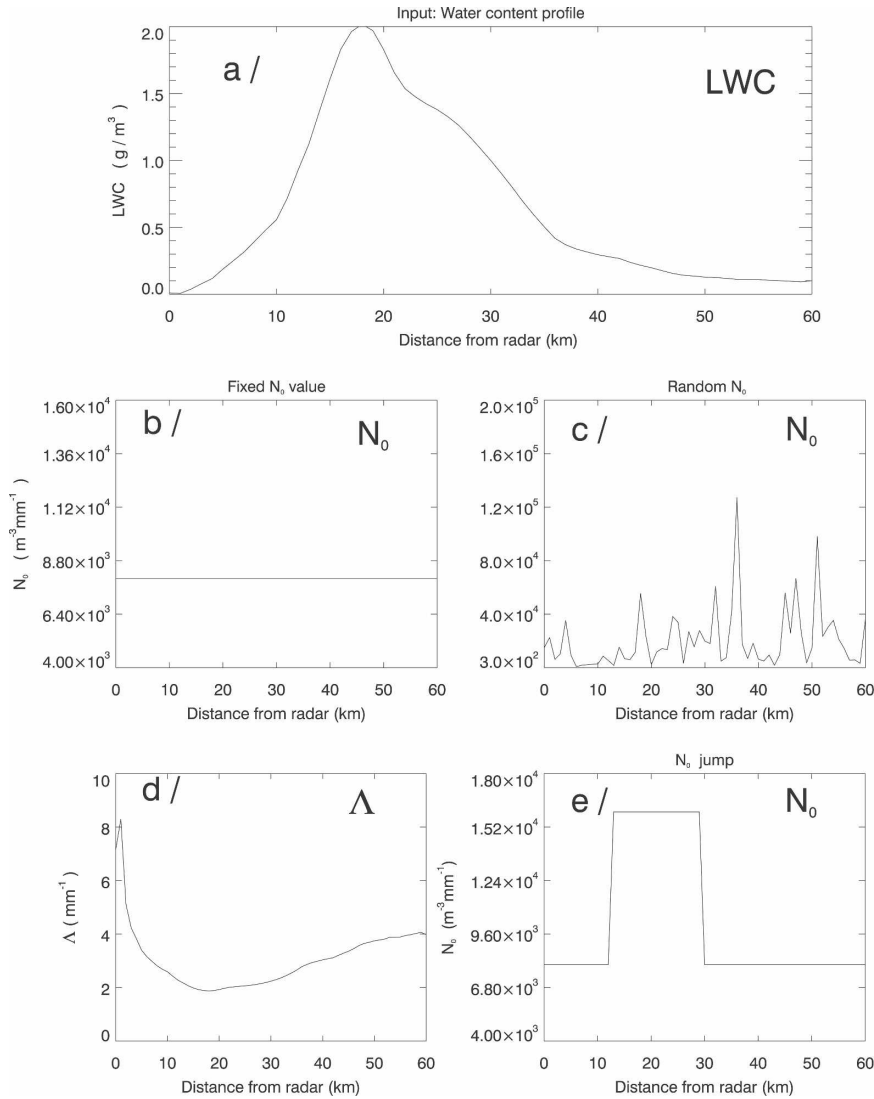
FIG. 2. Example along a given radial, of (a) the range profiles of water content; (b), (c), (e) the intercept parameter N_0; (d) and the slope of the DSD, calculated by the simulator at step 1. Here (b), (c), and (e) illustrate the various options that can be used to set N_0, as a fixed value, lognormally distributed around its mean or with parameterized jumps.

the SNR is high and rises sharply when the SNR decreases. The MOD "modulo" sign ensures that if the expression in bracket rises above π it is folded back between $-\pi$ and π. We adopted the following expression for $f(\text{SNR}) = \exp\langle 50\{1 - \exp[-(0.03/10^{0.1(\text{SNR})})]\}\rangle$, with SNR equal to $(Z_{Hm}\text{-MDR})$ in the simulator. An example is given in Fig. 3d, where two profiles of ϕ_{DP} are displayed, one without (dash line) and one with uncertainty $(\sigma_{\varepsilon_\phi} = 2°)$ added as in Eq. (5). It can be seen that, after 50 km, when the reflectivity falls below the MDR, ϕ_{DP} is extremely variable as expected for noise. As for the modeled uncertainty in Z, the uncertainty in ϕ_{DP} is uncorrelated from gate to gate or radial to radial.

(An example of simulated radar data, together with the original rain field, is illustrated in Fig. 9.)

For the radar data simulated in this paper the simulated radar has the following characteristics:

- Given that the horizontal resolution of the model output used here is only 2.5 km, there was no interest in simulating too high a resolution, so the radial resolution is 1 km and the radials are taken every 1.2°.
- The MDR at 10 km is −15 dBZ (a reasonable assumption for an X-band radar transmitting at 100 kW, with an antenna gain of 42 dB—beamwidth 1.2°—and a pulse width of 1 μs). We also carried out
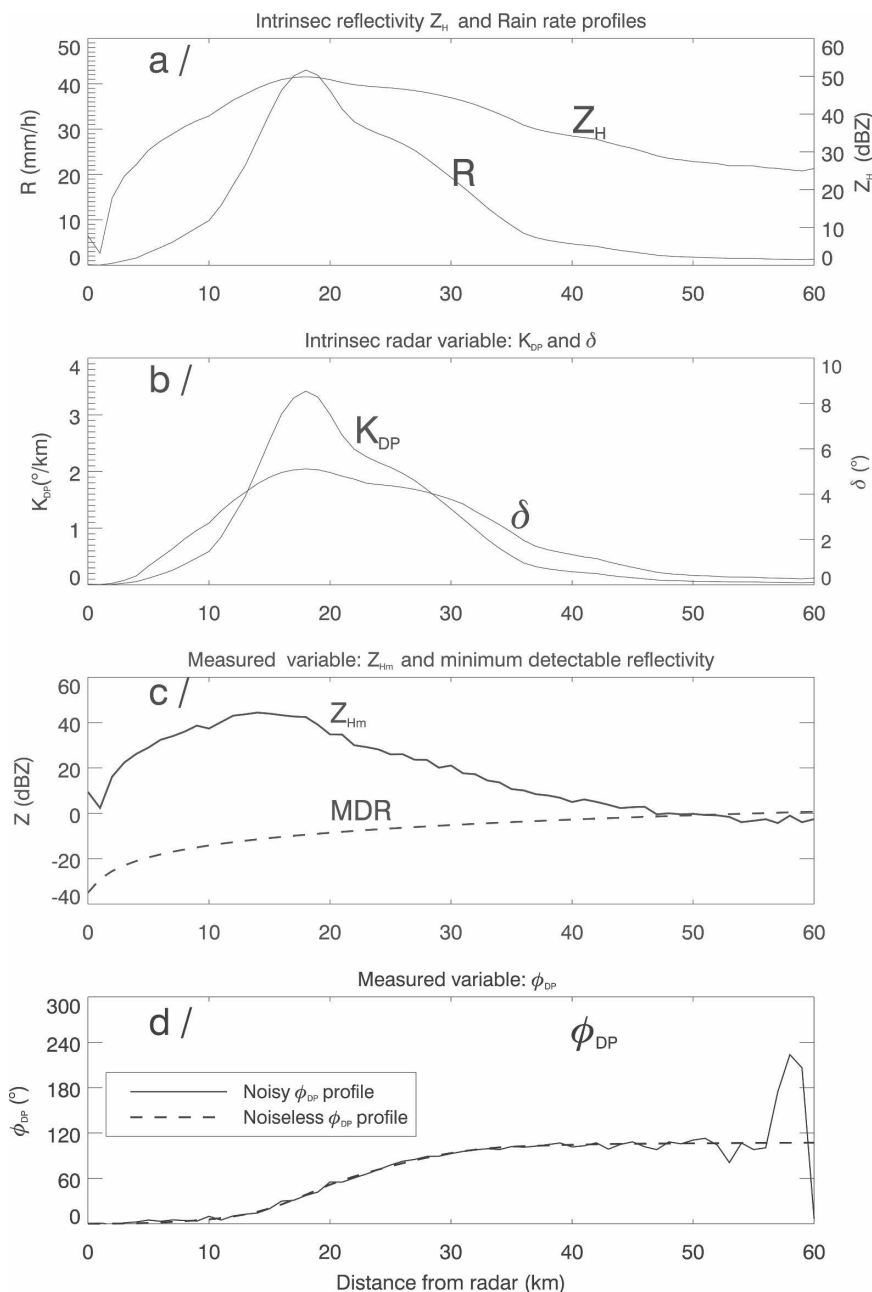
FIG. 3. (a), (b) Intrinsic variables and (c), (d) synthetic measurements produced by the simulator at step 2, for the water content profiles of Fig. 2. The variables are (a) the rain rate R and the intrinsic reflectivity in horizontal polarization Z_H; (b) the specific (K_{DP}) and backscattering (δ) differential phase shift; (c) the synthetic "measured" reflectivity Z_{Hm}, superimposed on the minimum detectable reflectivity MDR; (d) the synthetic "measured" differential phase shift, with (plain line) or without (dashed line) the measurement uncertainty module turned on. For this example the std dev in the error in Z is equal to 1 dBZ, and the std dev in ϕ_{DP} is equal to 2°.

tests with a higher value of MDR for the discussion on the maximum detection range presented in section 4e.

• The frequency used is 9.4 GHz.

Radar rain retrieval algorithms can now be tested on these variables and the result compared with the original rain profiles (Fig. 4). An example of rain retrieval for a given realization of the simulator and the same
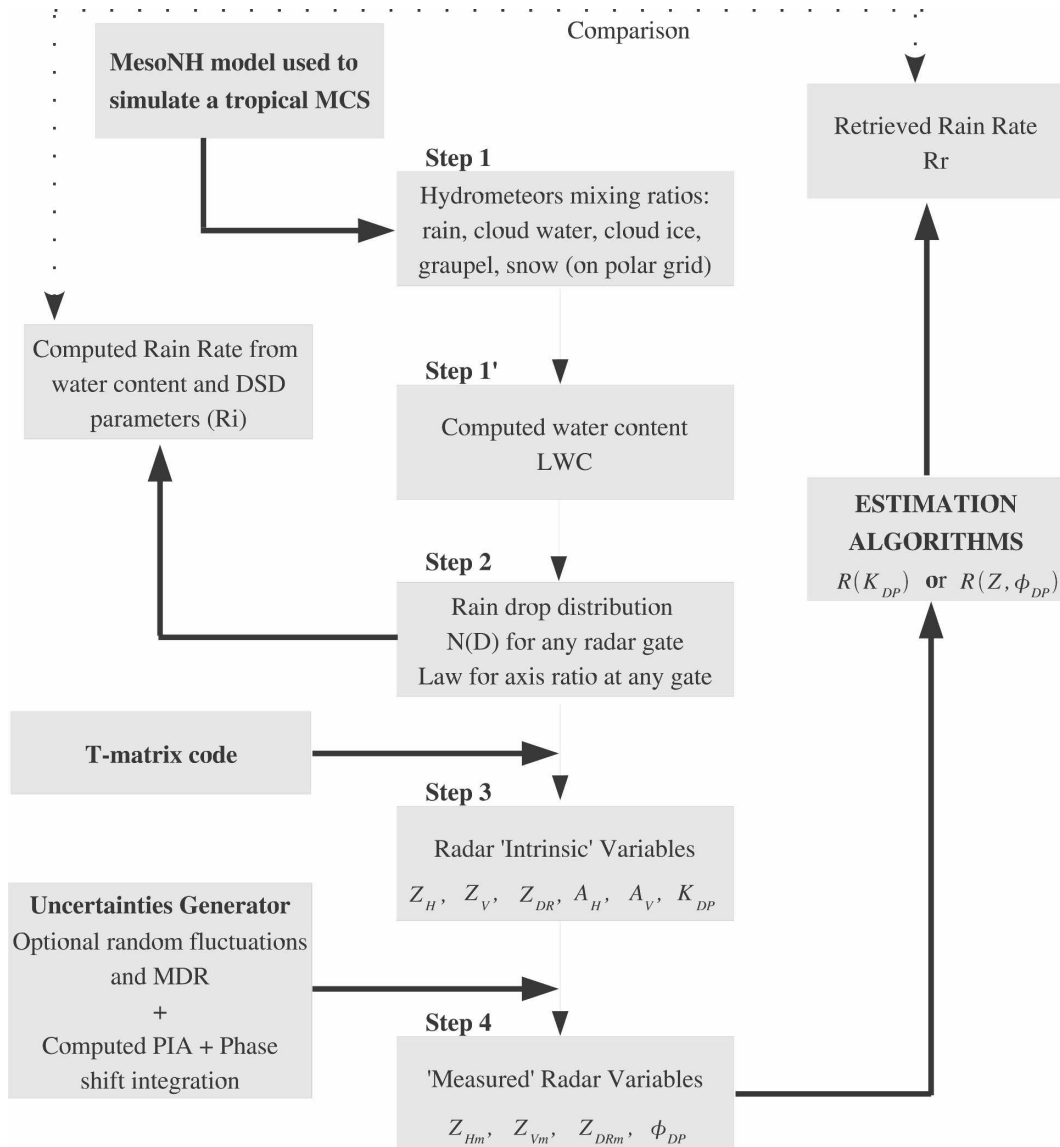
FIG. 4. This diagram summarizes the simulation setup and its use for analyzing rain retrieval schemes.

profile as in Figs. 2 and 3 is given in Fig. 5. The details of the retrieval schemes are given in section 3.

3. Rain retrieval schemes and natural variability of their coefficients

As discussed in the introduction, several schemes that use polarimetric radar variables have been proposed recently—and some of them tested—at X band. These schemes use one or a combination of the measured variables Z_H, ϕ_{DP}, or Z_{DR}. Sauvageot (1996) proposed a method that uses both reflectivity in one channel—say, Z_H—and the differential reflectivity Z_{DR}. The scheme matches two independent estimates of the

rain profile (one obtained from Z_H the other one from Z_{DR}, both corrected for attenuation by an iterative process) and adjusts the radar calibration. Smyth and Illingworth (1998) evaluated of the path attenuation through an estimate of the differential attenuation at the far side of a cell. It is assumed that "behind" a cell the rainfall is low and Z_{DR} should be zero so that a negative Z_{DR} is an indication of differential attenuation. Matrosov et al. (2005) also make use of Z_{DR} in their scheme. In their method the rain drops aspect ratio is parameterized and the oblateness retrieved via a power-law combination of Z_{DR}, K_{DP}, and Z_H. The scheme leads to an estimate of the rain rate supposed to be immune to the drop shape variability. However, we
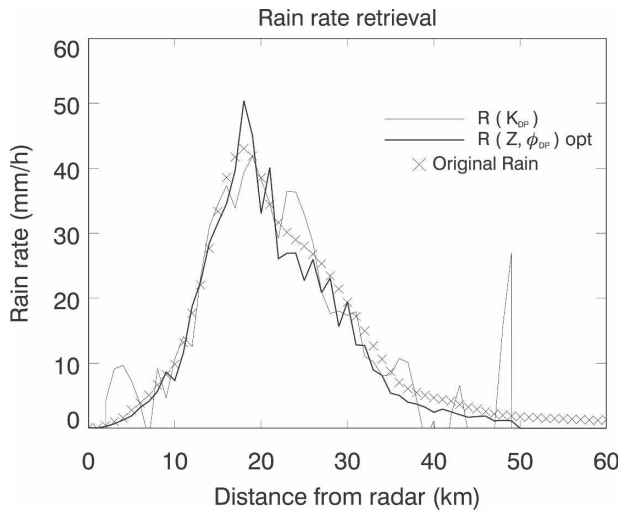
Rain rate retrieval

FIG. 5. Example of the rain profiles retrieved after application of the two retrieval schemes $R(K_{DP})$ and $R(Z, \phi_{DP})_{opt}$ on the synthetic radar variables of Fig. 3.

decided for the present study to concentrate on the schemes that use only the differential phase shift ϕ_{DP} and the reflectivity in one channel. The first reason is that we find that the relationship between Z_{DR} and other variables is dependent on too many factors (drops shape, DSD shape, spectrum maximum diameter, temperature, range of rainfall rates considered) to bring unambiguous information. The fact is well illustrated on the Fig. 6f, where it is seen that Z_{DR} is highly sensitive to the oblateness law of drops and also more sensitive than any of the other parameters to the shape of the drop size distribution (parameter μ) and also to the maximum diameter considered in the distribution (parameter D_{max}). We find also that the Smyth and Illingworth (1998) scheme might be difficult to implement at X band because of the limited range. All these factors made us restrict our preparatory study to the schemes that use either only ϕ_{DP} or a combination of ϕ_{DP} and Z_H.

a. Scheme 1: Direct use of a $R(K_{DP})$ relationship

It has been shown by many authors (Brandes et al. 2001; Bringi and Chandrasekar 2001; Matrosov et al. 1999) that the specific differential phase shift and the rain rate are well correlated and that their relationship is less sensitive to DSD variability than the classic Z–R relationship. Here K_{DP} is also immune to attenuation and unaffected by calibration and beam blockage. It is also known that one problem in the direct use of a R–K_{DP} relationship is that K_{DP} is estimated in practice by differentiating the "noisy" variable ϕ_{DP}, leading to a lack of precision. Several authors (Matrosov et al. 1999,

2002; Testud et al. 2000) have pointed out, however, that the problem is less acute at high frequencies, because for a given rain rate, K_{DP} increases approximately as the frequency and is a stronger signal at X band than at S or C band. In addition to the noise in ϕ_{DP}, the other problem that might affect the estimation of K_{DP} is the contribution of the scattering phase shift δ as well as the effects of cross-beam gradients (Ryzhkov and Zrnic 1998; Gosset 2004). However, the measurements that have been made at X band (Matrosov et al. 1999, 2002; Anagnostou et al. 2004) show no evidence of strong δ contamination on real data.

To implement this scheme on our synthetic data, K_{DP} is estimated by running a least square linear fit over the values of ϕ_{DP} from a number N of consecutive gates, where N can be chosen.

In theory K_{DP} is positive. This is assumed when using a simple power-law relationship to retrieve the rain rate. However, the noise in ϕ_{DP} can produce negative values of K_{DP}. To avoid introducing a positive bias by suppressing only negative spurious K_{DP}s, we use the formulation proposed by Sachidananda and Zrnić (1987):

$$R = \text{sign}(K_{DP}) a_{R-K_{dp}} |K_{DP}|^{b_{R-K_{dp}}}, \qquad (6)$$

with R in mm h^{-1}, the function sign is equal to 1 for positive numbers and -1 otherwise. Here $a_{R-K_{dp}}$ and $b_{R-K_{dp}}$ are the coefficient and exponent of the power-law relationship between R and K_{DP}. Their value at X band and their variability are discussed below in the section 3c and illustrated on the Fig. 7d.

b. Scheme 2: Correction attenuation using ϕ_{DP} and Z_H

The other type of usage that has been proposed for ϕ_{DP} is to exploit the high correlation between ϕ_{DP} measured between two range gates, and the attenuation integrated over the same path (Bringi and Chandrasekar 2001; Matrosov et al. 2002, 2005; Testud at al. 2000; Park et al. 2005a,b). As discussed by several authors (Bringi et al. 1990; Testud et al. 2000; Matrosov et al. 2002, 2005) and illustrated in Figs. 6a and 7a, the relationship between K_{DP} and the specific attenuation A_H (for horizontal polarization) is quasi-linear so that the path-integrated attenuation (PIA) can be approximated from the path-integrated ϕ_{DP} with a relationship of the type:

$$\text{PIA}(r_1, r_2) = a_{A-K_{dp}}[\phi_{DP}(r_2) - \phi_{DP}(r_1)], \qquad (7)$$

where r_1 and r_2 are the first and the last range of the path integration. The advantage of such a use is that ϕ_{DP} does not need to be differentiated.
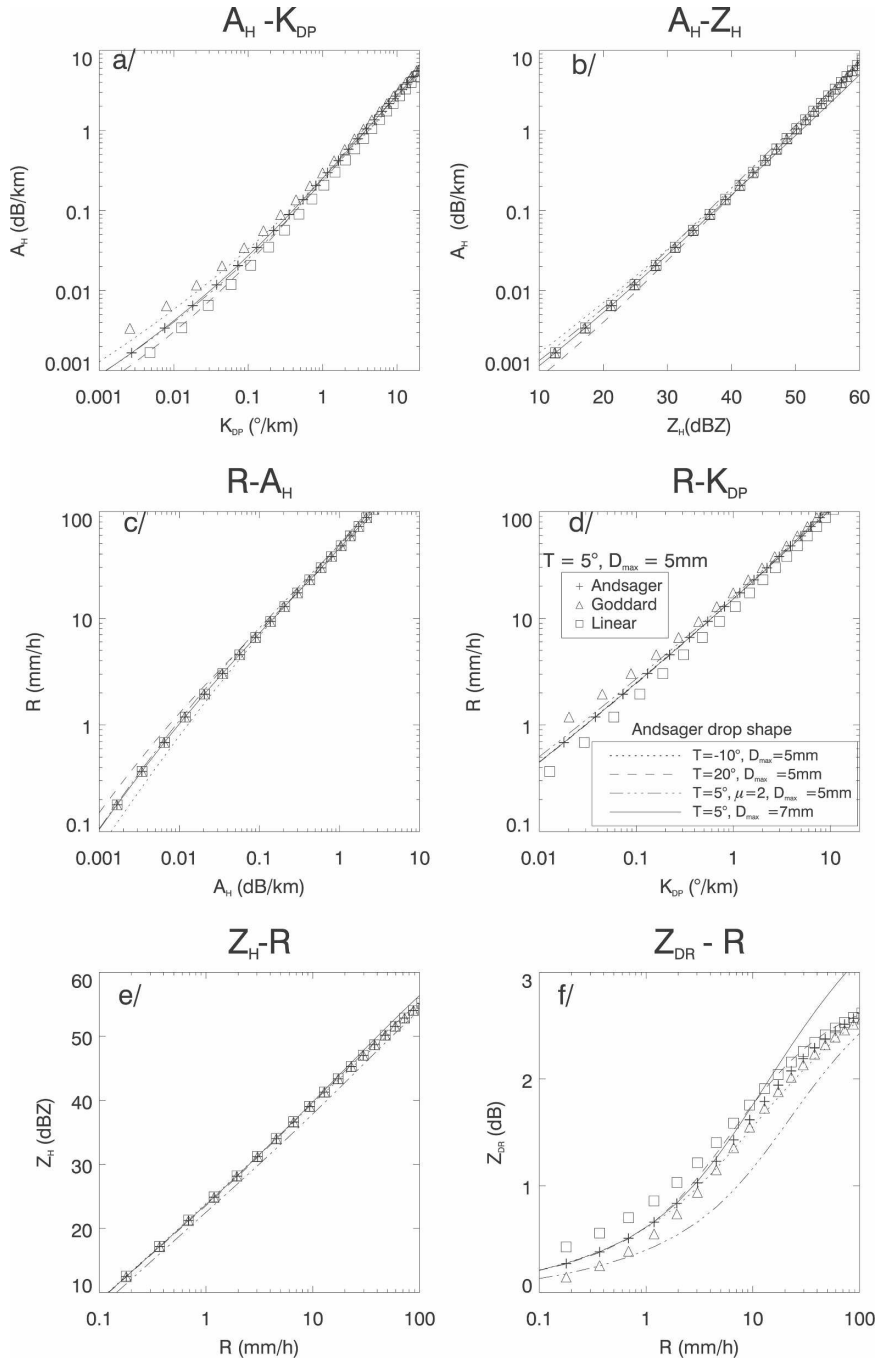
FIG. 6. Illustration of the variability of the relationships between couples of variables: (a) A_H–K_{DP}, (b) A_H–Z_H, (c) R–A_H, (d) R–K_{DP}, (e) Z_H–R, and (f) Z_{DR}–R. The calculations are made with a T-matrix code for normalized gamma distributions. Three oblateness laws cited in the text are used and labeled as Andsager, Goddard, and linear. The default values for the DSD are shape parameter $\mu = 0$, maximum drop diameter $D_{max} = 5$ mm, oblateness law at Andsager, and temperature $T = 5°$. The curves with symbols are for the three oblateness laws, as indicated, and the default values of T and μ. The dash and long-dash line are for the default oblateness law and μ, and two values of T: $-10°$ (short dash); $20°$ (long dash). The three-dotted–dash line is for the default values of oblateness, D_{max} and T, but $\mu = 2$. The plain line is for the default DSD and oblateness but with the maximum diameter $D_{max} = 7$ mm.
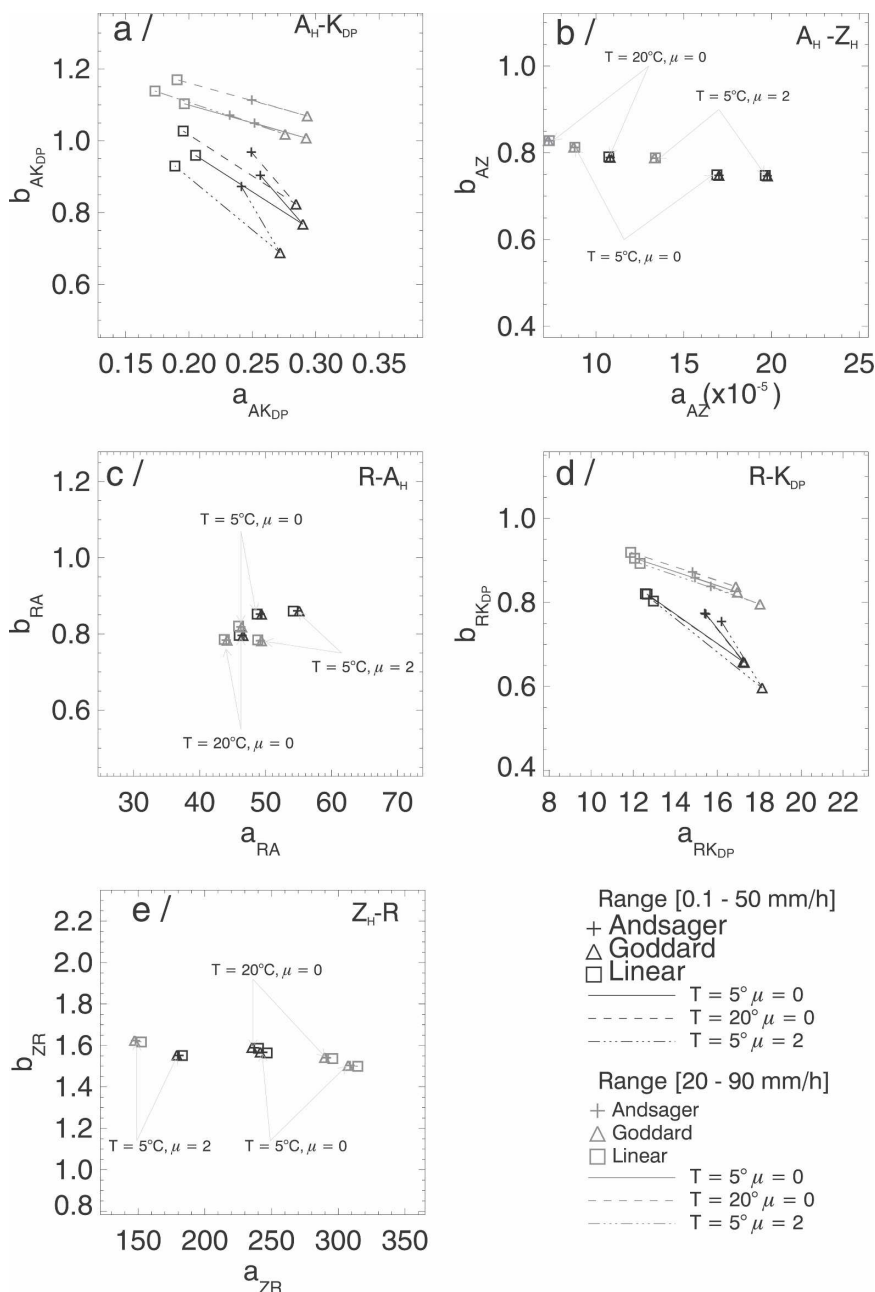
FIG. 7. Illustration of the variability of the coefficients a and the exponent b, of a $Y = aX^b$ fit on the curves of Fig. 6. The calculations are for two ranges of R: 0.1–50 mm h^{-1} in black and 20–90 mm h^{-1} in light gray. As in Fig. 6, the symbols are for the three oblateness laws and the line between the symbols indicates the value of T and/or the value of μ.

From this principle several schemes have been proposed. In Matrosov et al. (2002, 2005), the values of Z_H and Z_{DR} at each gate are corrected using the value of ϕ_{DP} and Eq. (7) and a similar one between the differential attenuation and ϕ_{DP}. Then, the rain rate is estimated from a combined polarimetric estimator as a function of K_{DP} and of the corrected Z_H and Z_{DR}.

Testud et al. (2000) and Anagnostou et al. (2004) use a different approach. Once the PIA is estimated from (7), the rain rate at each gate along the path is retrieved with a profiling technique such as the ones used for space radars (Marzoug and Amayenc 1991).

The basic principle of such algorithms is the existence of a power-law relationship,

$$A_H = a_{A-Z}Z^{b_{A-Z}}, \qquad (8)$$

between the specific attenuation and the reflectivity. It has been demonstrated (Hitschfeld and Bordan 1954; Marzoug and Amayenc 1991) that such an assumption and Eq. (3) lead to the following integral equation between the intrinsic and measured reflectivities, between two radar ranges r_1 and r_2:

$$\left(\frac{Z_m/dC}{Z}\right)^b(r_2) - \left(\frac{Z_m/dC}{Z}\right)^b(r_1) = -0.46a_{A-Z}b_{A-Z}$$

$$\int_{r_1}^{r_2} [Z_m(s)/dC]^{b_{A-Z}} ds, \qquad (9)$$

with dC, a miscalibration factor, set to 1 if the calibration is thought to be correct, and which can be retrieved by the scheme otherwise [see Eq. (12) below]. Noticing that the ratio of measured to intrinsic reflectivities, on the left-hand side, is a function of the PIA, the following expression is derived for the specific attenuation factor at range r:

$$A(r) = \frac{Z_m^{b_{A-Z}}[10^{b_{A-Z}0.1\text{PIA}(r_1,r_2)} - 1]}{\{I(r_1,r_2) + I(r,r_2)[10^{b_{A-Z}0.1\text{PIA}(r_1,r_2)} - 1]\}}, \quad \text{with}$$

$$(10)$$

$$I(r_1,r_2) = 0.46b_{A-Z}\int_{r_1}^{r_2} Z_m(s)^{b_{A-Z}} ds. \qquad (11)$$

As noticed before (Marzoug and Amayenc 1991; Testud et al. 2000), such an estimate of $A(r)$ is independent of the a_{A-Z} coefficient and immune to calibration problems. If the PIA is expressed as a function of $\Delta\phi = \phi_{\text{DP}}(r_2) - \phi_{\text{DP}}(r_1)$ as in (7), then we retrieve the expression of Testud et al. (2000) or Anagnostou et al. (2004).

Once the specific attenuation is estimated at each gate, the rain rate can be derived from an R–A relationship.

It is also noteworthy that if the PIA at range (r_1) is known (or best, equal to 0), Eq. (9) provides a constraint to adjust dC or a_{A-Z} (depending which assumption is made):

$$\frac{[10^{-b_{A-Z}0.1\text{PIA}(O,r_{11})} - 10^{-b_{A-Z}0.1\text{PIA}(O,r_2)}]}{I(r_1,r_2)} = \frac{a_{A-Z}}{dC^{b_{A-Z}}}.$$

$$(12)$$

If, in addition, it is assumed that the calibration is correct ($dC = 1$) and that a_{A-Z} depends only on N_0 (as in Testud et al. 2000 and Anagnostou et al. 2004), then Eq. (12) can be used to estimate N_0 along the (r_1, r_2) path. In this case, the coefficient a_{R-A} corresponding to the adjusted N_0 can be used for the rain retrieval.

c. Natural variability of the radar variables and the power-law relationships

The rain retrieval schemes presented above are based on power-law relationships between two radar variables or between one radar variable and the rainfall rate. Some analysis of the variability of these relationships has been done by the authors who proposed the schemes used at X band (Matrosov et al. 1999, 2002; Park et al. 2005a,b) and especially in the comprehensive work by Testud et al. (2000). However, some aspects, such as the range of rain rates considered to derive the coefficients, the occurrence of big drops in the sampled volume, or the temperature dependence, are treated only partially at X band—they have been discussed more comprehensively for the C band (Zrnic et al. 2000; Carey et al. 2000). Also, the oblateness laws used by the various authors are not the same. In addition, as noticed by Illingworth and Blackman (2002), the derivation of such relationships is very sensitive to the model and parameterization of the DSD, so it is better to compare the various sources of variability at the same time and with the same model.

The "natural" variability of the following relationships—A_H–K_{DP}, A_H–Z_H, R–A_H, R–K_{DP}—used by the two selected schemes, is illustrated in Fig. 6. We also present the classical Z–R and the Z_{DR}–R relationship for reference. For these plots we used a T-matrix code for the properties of individual drops and then integrated over the DSD. The DSD is a three-parameter normalized gamma distribution [Eq. (1)] with N_0 set to 8000 mm^{-1} m^{-3}. The default is to perform the integrations between $D_{\text{min}} = 0.1$ and $D_{\text{max}} = 5$ mm in 0.1-mm steps. Plots are also presented with the parameter D_{max} set to 7 mm to study the influence of bigger drops in the spectrum. In Fig. 6 the calculations were performed for three temperatures: 5°—the default, −10°, and 20°, consistent with our tropical application, and for two values of μ: 0 and 2. We tested three drop oblateness laws:

- The one proposed by Andsager et al. [1999, their Eqs. (1) and (3)].
- The one cited by Illingworth and Blackman [2002, Eq. (15)] and originally proposed by Goddard et al. (1995), which is based on disdrometer and radar data comparisons.
- A linear shape [Matrosov et al. 2005, their Eq. (3)] with an adjustable parameter β set to 0.062 mm^{-1} by default. In section 4 we experiment by varying the β parameter within the radials as it might vary according to some authors (Gorgucci et al. 2000, 2001).

The multiplicative coefficients a and the exponents b obtained by linear fit of the curves of Fig. 6 are given in Fig. 7.

It is noteworthy that the different relationships show very different dependences on the parameters we tested. As expected, only the relationships that apply to differential polarimetric parameters show a dependence on the oblateness law. Only the two relationships involving the specific attenuation A_H show a relatively strong dependence on temperature, and it is more marked for the A_H–K_{DP} relationship. The relationships involving Z or Z_{DR} show a strong sensitivity to the shape of the DSD, and so does the A_H–K_{DP} but to a lesser extent. As expected from the change of slope of the curves represented in Fig. 6, the results of the linear fit are very sensitive to the range of rain rates used for the fit. This is generally true for the multiplicative factor a as well as for the exponent b. This should be kept in mind when choosing the coefficients for a given application (i.e., tropical rainfalls for our purpose). This also encourages caution when manipulating formulas that assume that the exponent b can be fixed.

The A_H–K_{DP} relationship is very sensitive to the oblateness law and to the temperature, with a strong dependence on the range of rain rates considered. However, when this relationship is used to derive the PIA from the path-integrated ϕ_{DP}, the contribution of all the rain rates are averaged by the range integration, so that we expect the relationship between PIA and ϕ_{DP} to be more stable than suggested by the Figs. 6a and 7a.

The A–Z relationship (here A_H–Z_H) is also variable, but its exponent is mostly stable. As the retrieval of the specific attenuation using Eq. (10) uses only b_{A-Z} it is not affected by the A–Z variability. However, Figs. 6b and 7b show that the coefficient a_{A-Z} varies with temperature, as well as with μ and the median diameter (or, in Fig. 6, the rain range as we work with a fixed N_0). We have also tested the sensitivity of the relationships to the bigger drops of the DSD, by modifying the maximum diameter of integration, D_{max}, from 5 to 7 mm. We found that the A–Z relationship was very sensitive, with a change of 50% in a_{A-Z}. This means that interpreting the variability of a_{A-Z} as an indicator of N_0 variability (Testud et al. 2000; Anagnostou et al. 2004) can be erroneous.

The R–A_H relationship is the most stable, both in a and b. As stated before, the plot is for $N_0 = 8000$ m^{-3} mm^{-1}. For another value of N_0, the coefficient a_{R-A} would be multiplied by $(N_0/8000)^{(1-b_{R-A})}$, with $(1-b_{R-A})$ close to 0.15, according to Fig. 7c. As an example, if N_0 is multiplied by 2, on average, the change in a_{R-A} is only by 10%.

As a summary, we expect that, in the profiler scheme $R(Z, \phi_{DP})$, the main source of uncertainty will be the estimation of the PIA from ϕ_{DP}. To reduce that uncertainty, we will try to estimate the PIA over long rather than short paths. For that reason, and also because of the sensitivity of a_{A-Z} to factors other than N_0 and because of the fact that R–A_H is very stable, we will not try to apply N_0 tuning or partitioning in our scheme.

The R–K_{DP} relationship shows very little dependence on temperature, DSD shape, and the existence of diameters bigger than 5 mm, but it does vary a lot according to the range of rain rates considered, and of course according to the oblateness law. This is why some authors try to determine the oblateness from triplets of (Z_H, Z_{DR}, K_{DP}) and then apply a parameterized R–K_{DP} relationship (Matrosov et al. 2005).

Figure 6f shows that the R–Z_{DR} relationship is only mildly dependent on temperature, but it is very sensitive to the drop oblateness law and extremely sensitive both to the DSD shape (parameter μ) and to the existence of drops with diameters above 5 mm. This, together with the difficulties of correcting for differential attenuation, made us choose not to use Z_{DR}, as the information contained in that variable is difficult to interpret quantitatively without ambiguity.

As discussed for many years in the literature, the R–Z relationship is variable, and depends on temperature and DSD shape but only slightly on the mean diameter (illustrated here by the insensitivity to the rainfall rate range), as illustrated in Figs. 6e and 7e. As we generated the curves with a fixed value of N_0 the exponent is stable and close to 1.6 (thus similar to the value for S band, in the Rayleigh regime). With a similar reasoning to the above, we find that a change in N_0 means that a_{R-Z} is multiplied by $(N_0/8000)^{-0.6}$. For instance, a doubling of N_0 means that a_{R-Z} is reduced by 35%. In our scheme we will not use the R–Z relationship. In both the schemes we chose to use, the final estimation of the rainfall rate R is based on propagation parameters—that is, A_H in the case of the $R(Z, \phi_{DP})$ scheme and K_{DP} for the $R(K_{DP})$ scheme—whose relationships to R are shown to be more stable than for the backscattering parameters (Figs. 6 and 7).

4. Sensitivity tests

In this section, we use the simulation setup described in section 2 to carry out sensitivity tests on the two algorithms presented in section 3.

a. The numerical dataset

The dataset comes from an explicit simulation of a squall line using the mesoscale numerical model Meso-NH (Zahiri 2007; Diongue et al. 2002). An intense squall line—actually observed during the 1992 Hydrological Atmospheric Pilot Experiment (HAPEX) Sahel campaign (Goutorbe et al. 1994)—is simulated. A grid nesting method is used to keep the benefit of a cloud-
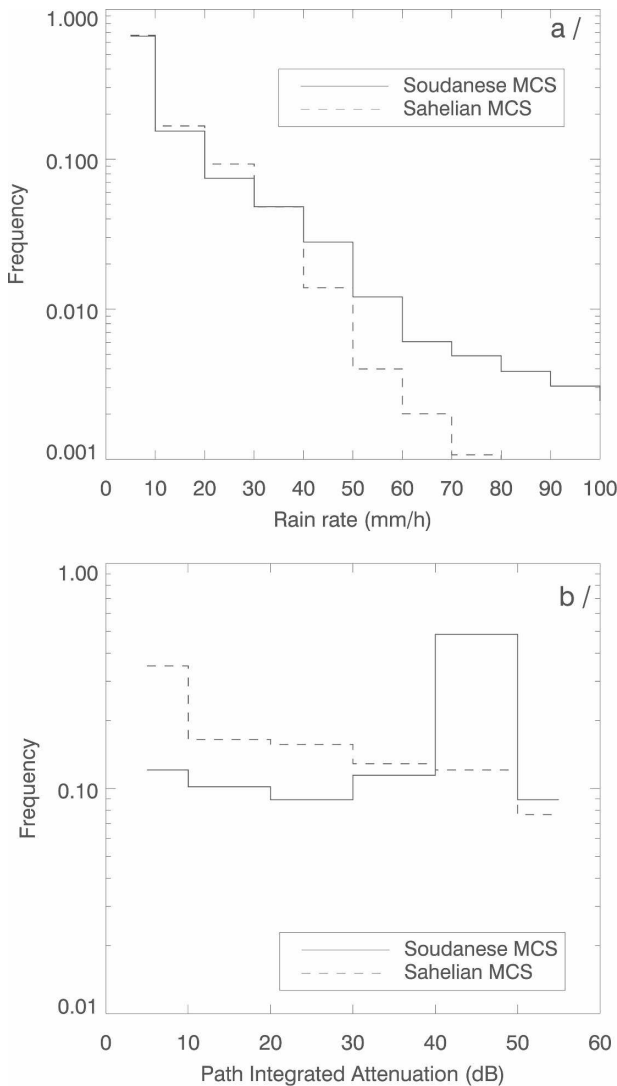
FIG. 8. Main characteristics of the precipitation fields the virtual radar is scanning, for two positions of the radar, which are labeled Sahelian and Sudanese. (a) The probability distribution of the rain rate is illustrated. (b) The distribution of the values of the PIA, over all the radials of the 12 PPIs of each zone, is illustrated.

resolving model resolution. The high-resolution model has a 2.5-km horizontal resolution and covers an area of about 800 km × 800 km.

The radar was positioned in two locations within that domain, and in each position 12 plan position indicator (PPI) scans, 5 min apart, were simulated. The distribution of the rain rates in the area covered by each "radar" for the 2 h of exploration is illustrated in Fig. 8a. To qualify the numerical dataset, the distribution of radar observed PIA is also given in Fig. 8b. For both areas and especially for the southern one [Sudanese mesoscale convective system (MCS)], intense precipitations are sampled, as shown in Fig. 8. Over the dif-

ferent radials a good variety of PIA or rain rates is sampled.

An example of the synthetic radar data, with the original rain field, the simulated reflectivity (Z_H), and the differential phase shift (ϕ_{DP}), is given in Fig. 9. This is obtained with the radar configuration described in section 2: the radar frequency is 9.4 GHz, the minimum detectable reflectivity (MDR) is set to −15 dBZ at 10 km, the range resolution is 1 km, and the radials are 1.2° apart in azimuth. The effect of the strong attenuation of the radar wave by rain, at X band, is visible on the simulated reflectivity (Fig. 9b): the rain cells located beyond 50 km from the radar, to the east, have a reflectivity below the MDR and do not appear on the Z_H field. The disappearance of these cells due to attenuation is also visible on the ϕ_{DP} pattern (Fig. 9c), which is very noisy because the signal is below detection.

b. Options for the direct model

As explained in section 2, the simulator is modular and several options can be chosen for generating the synthetic radar data.

1) REFERENCE MODEL

For the default or reference simulation, the DSD for each gate is calculated with Eqs. (1) and (2), and the value of the intercept parameter N_0 is set to 8000 mm^{-1}m^{-3}, as it is in the Meso-NH microphysical scheme. The default oblateness law is the one by Andsager et al. (1999). The measurement uncertainty is switched off. This is the synthetic dataset on which we expect the algorithms to work best.

2) MEASUREMENT UNCERTAINTY

For our dataset, the MDR is set to −15 dBZ at 10 km, as mentioned before. When the measurement uncertainty option is switched on, the standard deviation of the error on Z {σ_{ε_Z}, defined in section 2b is set to 1 dBZ, and the one on ϕ_{DP} [$\sigma_{\varepsilon_\phi}$, Eq. (5)] is set to 2°}.

3) GATE-TO-GATE VARIABILITY OF THE DROP ASPECT RATIO

Several studies (Gorgucci et al. 2000, 2001) have suggested that the mean oblateness of drops might vary from gate to gate. Even though such an idea is not consensual in the weather radar community, it is interesting to test this effect on the retrieval schemes. The gate-to-gate variability of the aspect ratio is imposed here with a very simple model. The linear oblateness law defined by an aspect ratio r_a equal to $r_a(D) = 1. +$
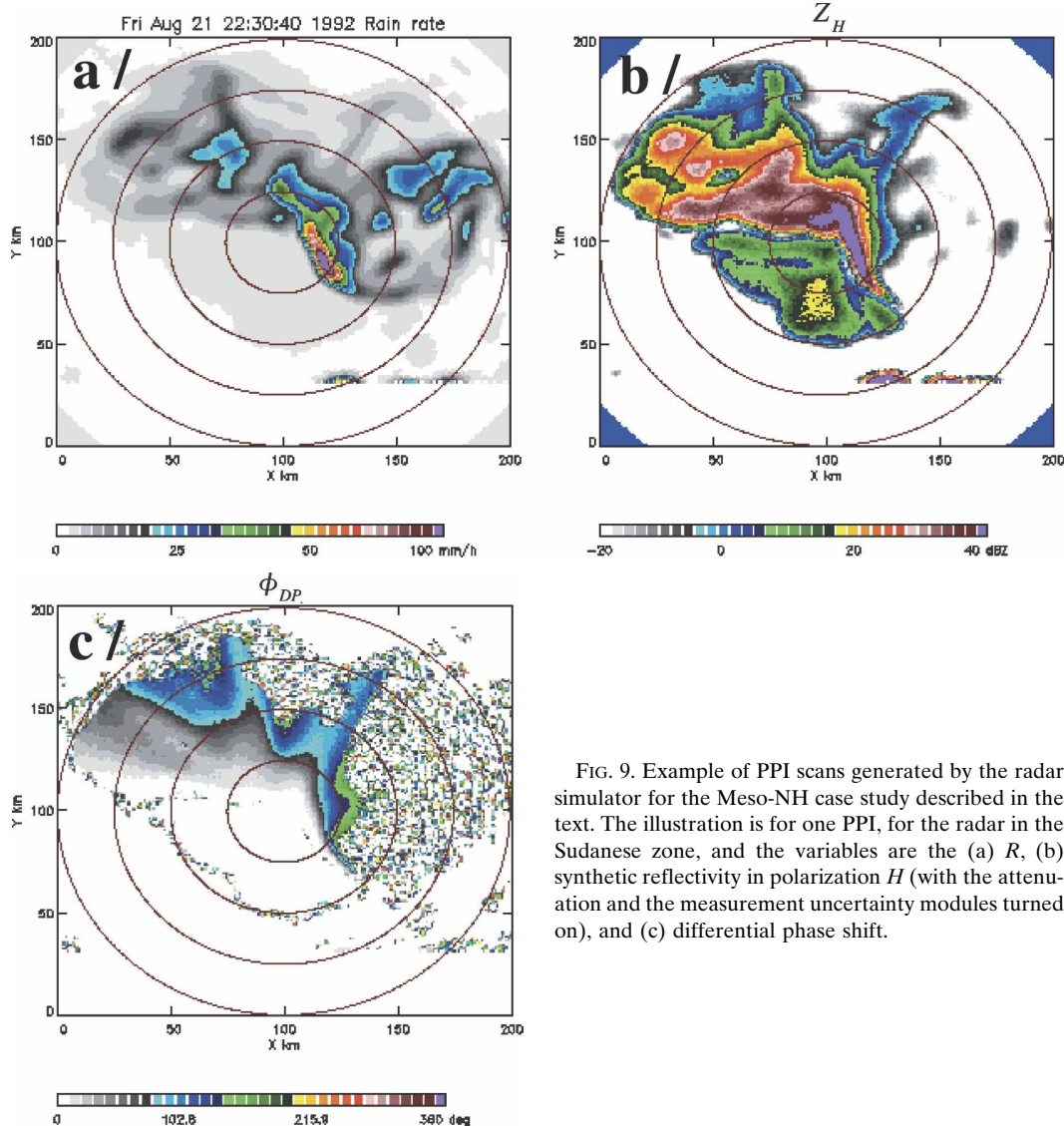
FIG. 9. Example of PPI scans generated by the radar simulator for the Meso-NH case study described in the text. The illustration is for one PPI, for the radar in the Sudanese zone, and the variables are the (a) R, (b) synthetic reflectivity in polarization H (with the attenuation and the measurement uncertainty modules turned on), and (c) differential phase shift.

$\beta(0.5 - D)$ for D above 0.5 mm is adopted, and β can take any value among (0.052, 0.057, 0.062, 0.067, 0.072). The values of β are decorrelated in range and from one radial to the next.

4) OCCURRENCE OF LARGE DROPS IN THE RADAR RESOLUTION VOLUME

The default value of the maximum diameter considered for the integration over the drop size spectrum is set to $D_{max} = 5$ mm. Most of the disdrometers available currently (Miriovsky et al. 2004) do not measure drops above this size. However, Carey et al. (2000) have observed that the coefficient of proportionality between K_{DP} and the specific attenuation (our a_{A-Kdp}) was stronger than predicted from calculations and pointed out the possible influence of the larger drops of the spectrum. To study the sensitivity of the algorithms to a discrepancy between the actual drop spectrum width and the one that was assumed when setting the coefficients (a_{A-Z}, b_{A-Z}, a_{A-Kdp}, a_{R-A}, b_{R-A}, a_{R-Kdp}, b_{R-Kdp}), we include drops up to $D_{max} = 7$ mm in our direct model. (The corresponding simulation is labeled "big drop" on the Figs. 12–17.)

5) GATE-TO-GATE VARIABILITY OF THE INTERCEPT PARAMETER: PARAMETERIZED N_0 JUMP OR NORMAL DISTRIBUTION

A gate-to-gate variability of N_0 can be introduced, still respecting the water content constraint [Eq. (2)]. Two models of variation are envisaged:

- The N_0 "jump" as reported by several authors (Wald-vogel 1974; Uijlenhoet et al. 2003): this is set by imposing a jump of N_0 from the default value, whenever the water content is above a given threshold. From observations, it was decided to impose a value of $N_0 = 16000\ \mathrm{m}^{-3}\ \mathrm{mm}^{-1}$ for LWC greater than $1\ \mathrm{g}\ \mathrm{m}^{-3}$ (as in Fig. 2e).

- The N_0 gate-to-gate random variability (as in Fig. 2c): that model is close to what is actually observed with disdrometers. A random number generator (Box–Mueller method) and an auto-regressive scheme (order 1) are used to impose the probability density function (pdf) of N_0 over the entire scan and its spatial correlation. A decorrelation distance is imposed only along the range axis, while the radials are decorrelated.

An example of the pdf of the logarithm of N_0 is illustrated in Fig. 10a. It can be seen that it reproduces well a Gaussian pdf. Figure 10b illustrates the decorrelation of N_0 with distance (here with a decorrelation distance of 6 km). We tested two values for the decorrelation distance (2 or 6 km). It can be seen in Fig. 10b that the scheme respects well the exponential decorrelation model.

Note that whatever the direct model, we always use at each gate the temperature of the mesoscale model at the corresponding level; so the effects of the variability of temperature within the PPI is always included. However this effect is weak in our case because we use low-level PPI and a short range.

We tested several combinations of the options above but for this work we focus only on the four models obtained by switching on the options one at a time; they are summarized in Table 1.

c. Options for the retrieval schemes

The two schemes proposed in section 3—that is, the profiling approach $R(Z, \phi_{DP})$, as in Eq. (10), and the direct use of a R–K_{DP} relationship, as in Eq. (6)—are applied to the five sets of synthetic data obtained with the options above (see Table 1). For the results presented here the $R(K_{DP})$ scheme is implemented by calculating K_{DP} by linear fit over five gates.

To implement the schemes we need to set the initial value of the parameters, that is, the four coefficients b_{A-Z}, a_{A-Kdp}, a_{R-A}, b_{R-A} for the scheme $R(Z, \phi_{DP})$ and the coefficients a_{R-Kdp}, b_{R-Kdp} for the $R(K_{DP})$ scheme. The usual method for setting initially these coefficients is by best fit, through values of Z_H, A_H, K_{DP}, and R calculated for DSDs of the type expected (or already
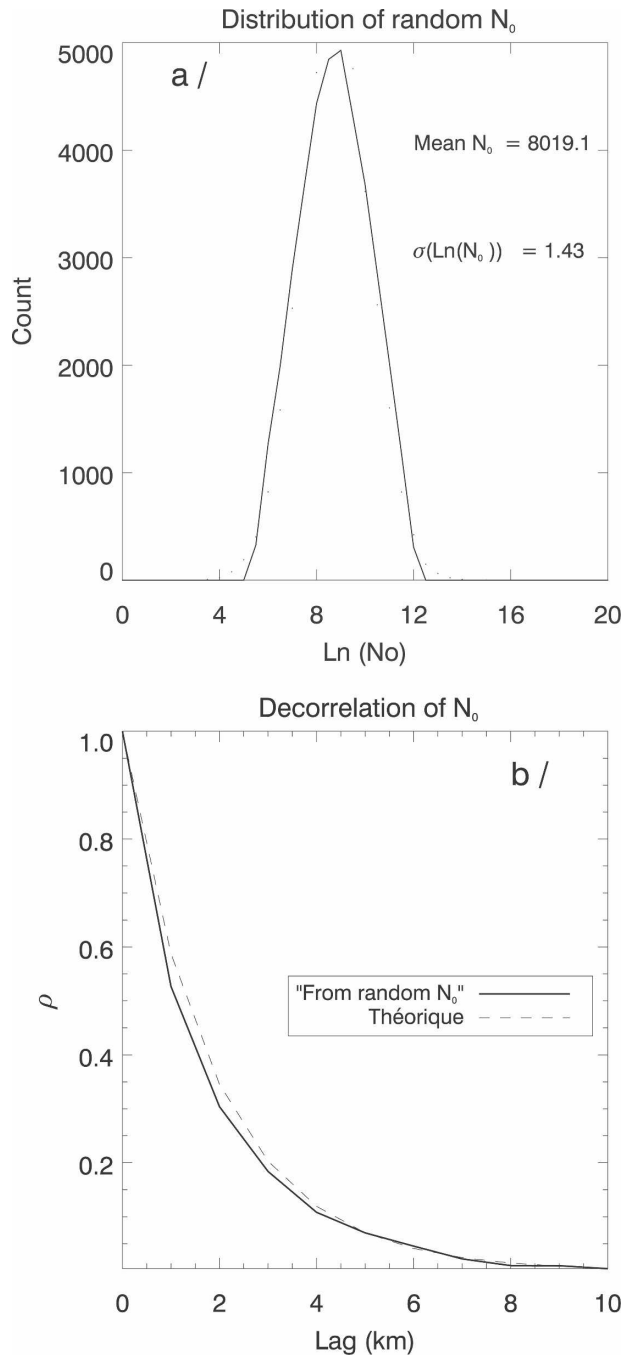
FIG. 10. Illustration of the N_0 random variability module. (a) An example of distribution of the $\log(N_0)$ over all the gates of a given PPI is shown, superimposed on the Gaussian distribution of same mean and std dev. (b) The decorrelation of N_0 with range (here with a decorrelation distance of 6 km) is shown, superimposed on the exponential model.

measured) in the region of interest. This is what we call setting the inverse model.

The natural variability of rainfall characteristics affects the adequacy of the inverse model in two ways: (i)

TABLE 1. Summary of the 30 simulation setups, obtained by applying combinations of five options in the direct model and for each of them, six choices in the retrieval scheme coefficients. The two schemes, $R(K_{DP})$ and $R(Z, \phi_{DP})$, and the option $R(Z, \phi_{DP})_{opt}$ are applied in the 30 cases and the scores are summarized in Figs. 13 and 14.

Direct model: Generation of synthetic radar variables

	Reference	Noise on	Aspect ratio random	Big drop	N_0 random
N_0	8000 m^{-3} mm^{-1}	8000 m^{-3} mm^{-1}	8000 m^{-3} mm^{-1}	8000 m^{-3} mm^{-1}	Lognormal pdf with mean, 8000 m^{-3} mm^{-1}
D_{max}	5 mm	5 mm	5 mm	7 mm	5 mm
Oblateness law	'Andsager'	'Andsager'	Linear with parameter b random	'Andsager'	'Andsager'
Measurement uncertainty	Off	On: 1 dBZ, 2°	Off	Off	Off

Assumption for retrieval scheme settings

N_0	8000 m^{-3} mm^{-1}														
Oblateness law	'And'	'Illin'	Lin 0.06	'And'	'Illin'	'Lin' 0.06	'And'	'Illin'	'Lin' 0.06	'And'	'Illin'	'Lin' 0.06	'And'	'Illin'	'Lin' 0.06
Rain rate range (0.1–50 mm h^{-1}) = 'Med' (20–90 mm h^{-1}) = 'High'	Med / High	Med / High	Med / High	Med / High	Med / High	Med / High	Med / High	Med / High	Med / High	Med / High	Med / High	Med / High	Med / High	Med / High	Med / High
Simulation number	1	2	3	4	5	6	7	8	9	10	11	12	13	14	15

As discussed in section 3 and by other authors (Berne and Uijlenhoet 2005) and visible in Fig. 6, the coefficients obtained by best fit are suited "on average," but they are not exact for the specific DSD observed at each gate or for the entire range of rain rates that might be observed. So, even if the drop shape, DSD shape, and N_0 are known, and the coefficients calculated accordingly, the inverse model is still imperfect. This is enhanced in the simulations where not only the rain rate but also N_0, the spectrum width, or the drop shape vary within the scans (as described in section 4b, options 3–5, above). In addition, in our direct model, the temperature varies within the scan as in Meso-NH. (ii) The other way the inverse model can mismatch the direct one is when the average characteristics of the DSDs are set erroneously. This will be tested by calculating the initial coefficients on DSDs that have different characteristics (oblateness law, parameter μ, and N_0) than the ones of the direct model.

Once the options for the oblateness law, the DSD shape, and the temperature are selected, the coefficients ($a_{A–Z}$, $b_{A–Z}$, $a_{A–Kdp}$, $a_{R–A}$, $b_{R–A}$, $a_{R–Kdp}$, $b_{R–Kdp}$) are calculated as in section 3c, by a linear fit over the chosen range of rain rates. As $b_{A–Kdp}$ is forced to 1 in our scheme, we calculate a_{A-Kdp} by fitting directly a linear function $A_H = a_{A–Kdp} K_{DP}$. To optimize the choice of $a_{A–Kdp}$, which was shown in section 3c to be very variable, we can also calculate it by fitting a function, $PIA = a_{A–Kdp} \phi_{DP}$, over the path-integrated values of attenuation and differential phase shift, of all the radials from all the PPIs of our simulations.

The profiling algorithm is called $R(Z, \phi_{DP})_{opt}$ in this case.

d. Test results

The overall principle of the tests is summarized on the schematic of Fig. 4. The scores of the two algorithms are presented here for 30 configurations of the simulation setup: five options for the direct model (reference, with "noise," with variable oblateness law, with "big drops," and with randomized N_0), and for each option six ways to calculate the coefficients of the algorithms are tested (three oblateness law and two rain-rate ranges). In addition, two options—$R(Z, \phi_{DP})$ and $R(Z, \phi_{DP})_{opt}$, described above—are used to calculate $a_{A–Kdp}$. The test configurations used for the present paper are summarized in Table 1.

Comparisons of the original rain rates to those retrieved with the two schemes $R(K_{DP})$ and $R(Z, \phi_{DP})_{opt}$, for a given PPI, are presented on the scatterplots of Figs. 11 and 12. These examples illustrate the effects of the five assumptions considered for the direct model. On each figure, the standard scores whose definition is recalled below are indicated. If the R_i represent the series of N initial rain rates and the E_i their estimate, the scores are as follows:

$$\text{Bias} = \sum_i (E_i - R_i); \qquad (13)$$

$$\text{normalized bias (NB)} = \frac{\sum_i (E_i - R_i)}{\sum_i R_i}; \qquad (14)$$

$$\text{normalized standard error (NSE)} = 100\% \frac{\sqrt{\sum_i (E_i - R_i)^2}}{\sum_i R_i}; \quad \text{and} \qquad (15)$$

$$\text{nash} = 1 - \frac{\sum_i (E_i - R_i)^2}{\sum_i \left(R_i - \frac{\sum_i R_i}{N} \right)}. \qquad (16)$$

On all the examples the scores are good compared to what would be found on real data because our dataset is by construction very "clean": no ground echoes or other targets, which is in practice the main source of error in radar data, no fluctuations of the transmitted power or malfunctioning of the automatic frequency control (AFC), no positioning uncertainty. This is an ideal radar. However, the exercise is interesting to

compare the relative contributions of the sources of uncertainty and also the behavior of both schemes. It can be seen also that the reference simulation is not perfect, and has a nonzero bias and standard deviation. As discussed in section 3, this is explained by the fact that the power-law relationships on which the schemes rely, are only true, in the best case, "on average," but not exact at each gate or for all the rain rates. This,
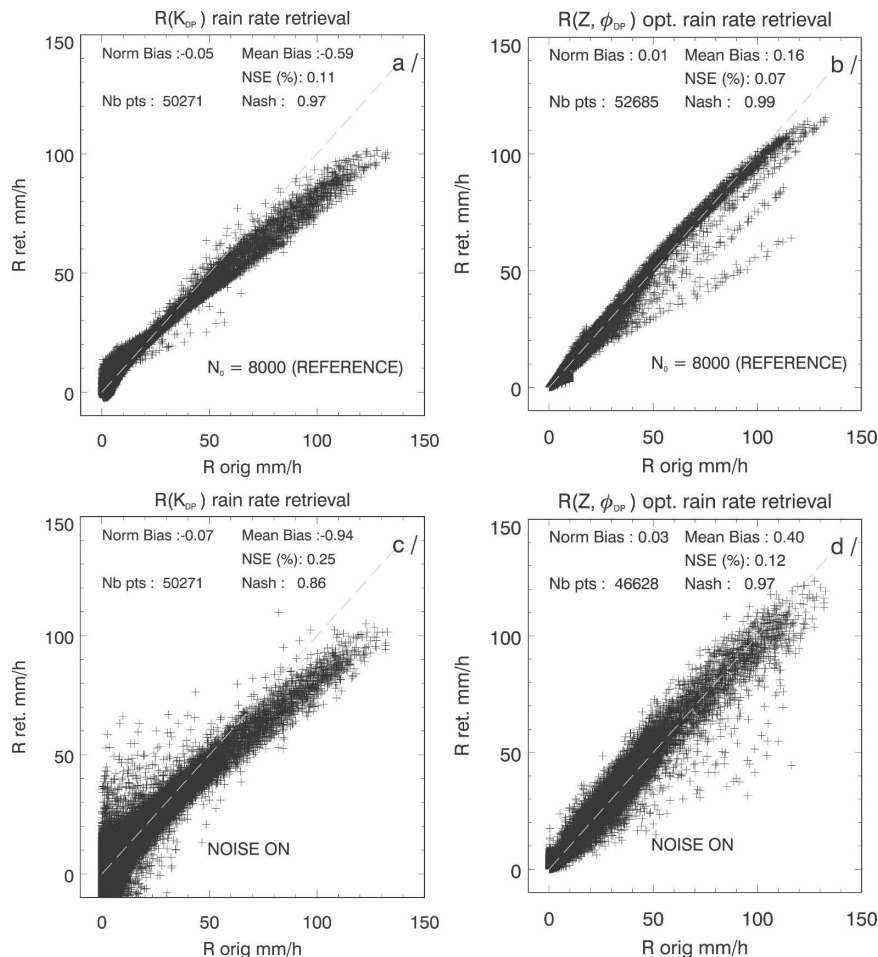
FIG. 11. Scatterplots of retrieved vs original R, after applying the two retrieval schemes to the synthetic radar data. Shown are (a), (c) the results for the scheme $R(K_{DP})$ and (b), (d) the ones for $R(Z, \phi_{DP})_{opt}$. Two settings of the direct model were used: the reference setting for (a) and (b) and the option with measurement uncertainty turned on in (c) and (d) (noise on). The standard scores (NB, mean bias, NSE, and Nash) are indicated in the figures.

together with smoothing effects, explains the tendency of both schemes to underestimate the higher rain rates. Indeed, the change of slopes observed toward the higher values, in both the A_H–K_{DP} and R–K_{DP} curves, in Figs. 6a or 6d, cannot be taken into account by a single set of coefficients a and b. Note also that the temperature within the PPI varies a little, as prescribed by Meso-NH.

In Figs. 13 and 14, the results are summarized in term of normalized bias and normalized standard error and compared for the whole set of simulations (Table 1). It can be seen that the worst results are obtained for the simulation with a gate-to-gate variability of the oblateness law. This is also the simulation where the benefit of adjusting the $a_{A–Kdp}$ coefficient on the PIA (ϕ_{DP}) rather than on the specific values (A_H, K_{DP}) is the most visible, as illustrated by the better scores of the $R(Z,$ $\phi_{DP})_{opt}$ scheme compared to the $R(Z, \phi_{DP})$ one. The effect of the largest rain drops is mainly sensitive for the $R(Z, \phi_{DP})$ scheme, which depends on the assumed value of $a_{A–Kdp}$. The other interesting finding is the sensitivity of the schemes to the random variability of the intercept parameter N_0 around its mean. The effect is equivalent or stronger than the effect of an uncertainty of 1 dBZ and 2° on reflectivity and differential phase shift, respectively. It is also found that the $R(K_{DP})$ scheme is more sensitive than the profiling one to the variability of the coefficients as a function of rain rate and also to noise. The tests show the superiority of the profiler $R(Z, \phi_{DP})$ scheme, when the PIA is obtained using coefficients that have been adjusted on the path-integrated propagation variables, as in the $R(Z,$ $\phi_{DP})_{opt}$ scheme. In practice, this could be obtained by having collocated measurements of ϕ_{DP} and of the path
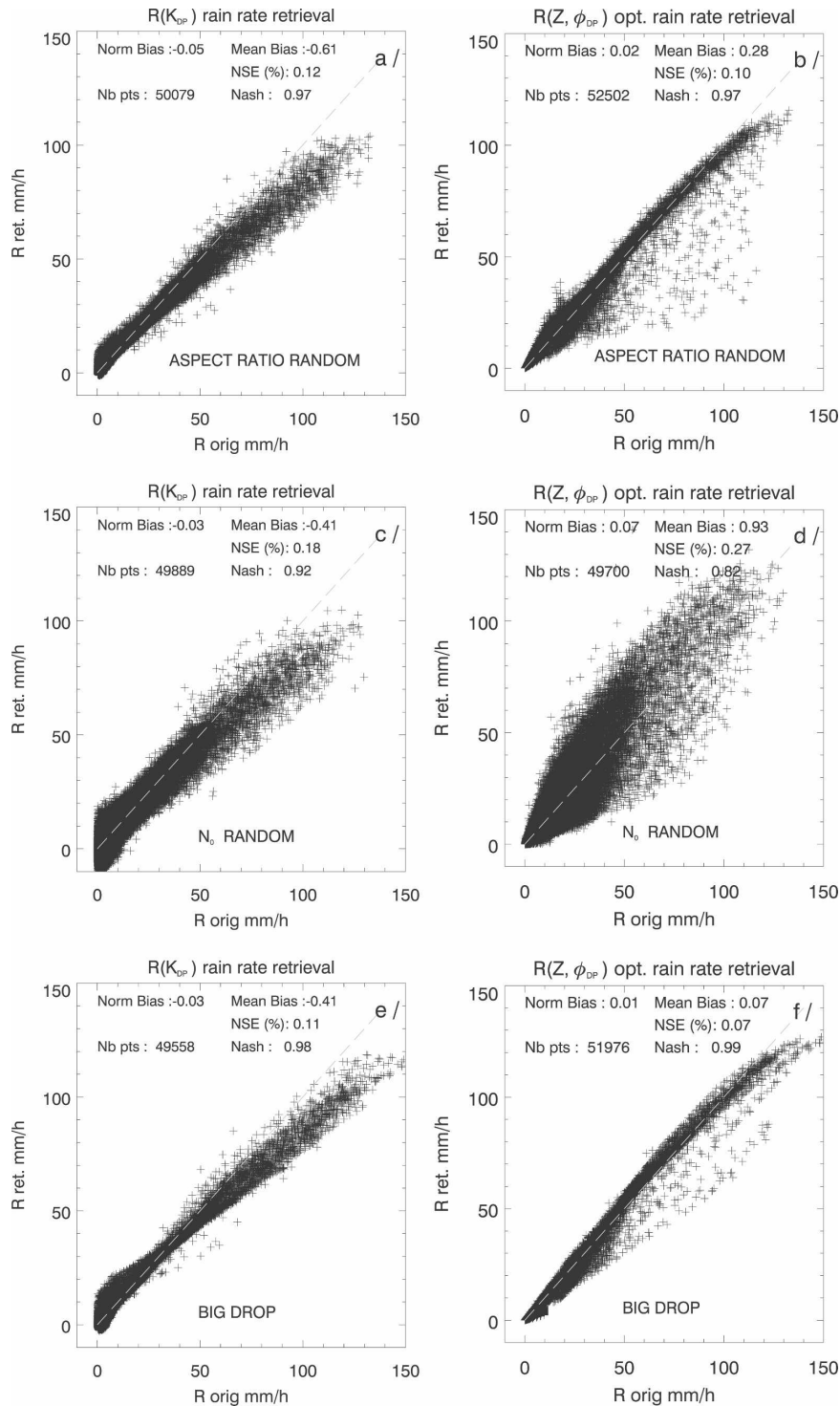
FIG. 12. Same as Fig. 11, but using the following options: (a), (b) random aspect ratio; (c),
(d) random variability of N_0; and (e), (f) big drops.

attenuation for a few radials—for instance using the mountain reference technique of Delrieu et al. (1997) or a microwave link as in Rahimi et al. (2003). This should bring a better adjustment of $a_{A-K\mathrm{dp}}$ than dis-

drometric measurements, which might misrepresent the amounts of the larger drops. The results illustrate the high sensitivity of the profiler scheme to a correct determination of the PIA from ϕ_{DP}, while the
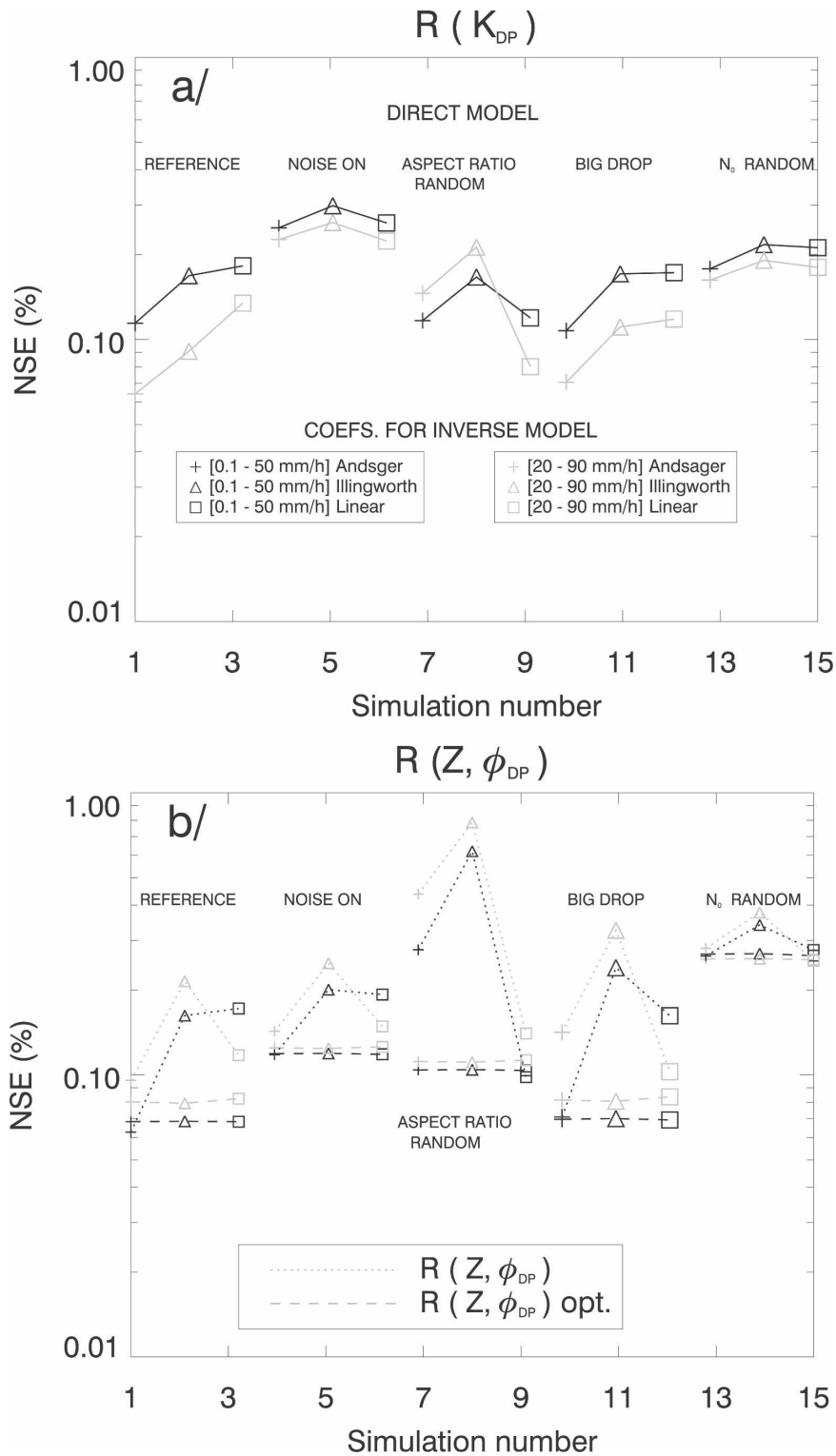
FIG. 13. NSE obtained for the different test configurations summarized in Table 1. (a) The score is indicated for the $R(K_{DP})$ scheme. (b) The results are for the two options, $R(Z, \phi_{DP})$ and $R(Z, \phi_{DP})_{opt}$, of the profiler scheme. The five possible settings for the direct model are indicated on the plots. The symbols indicate which oblateness law is used for the calculation of the algorithm coefficients. As indicated, the light gray and black lines show which range of rain rates was used to derive the coefficients of the retrieval schemes.
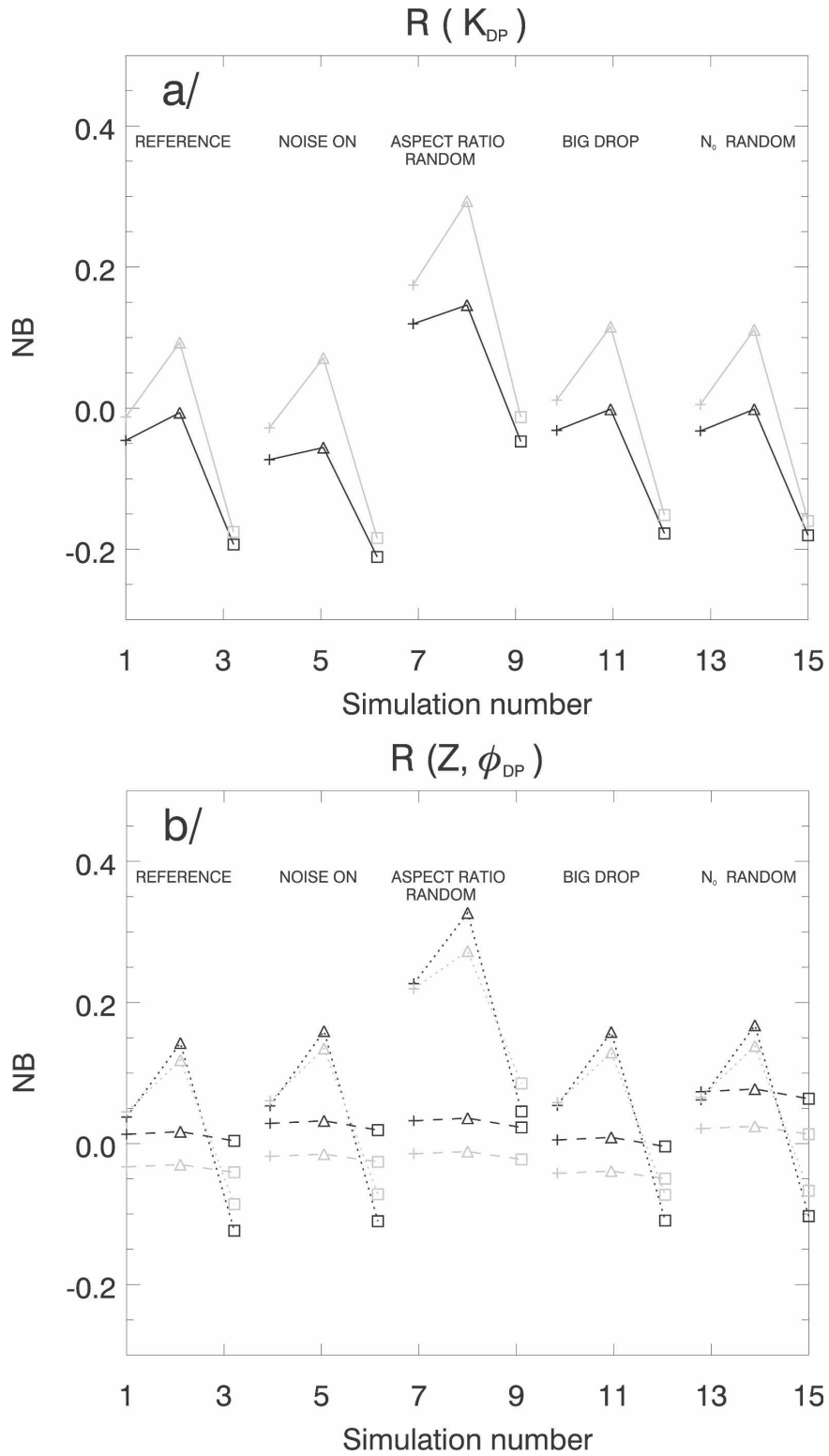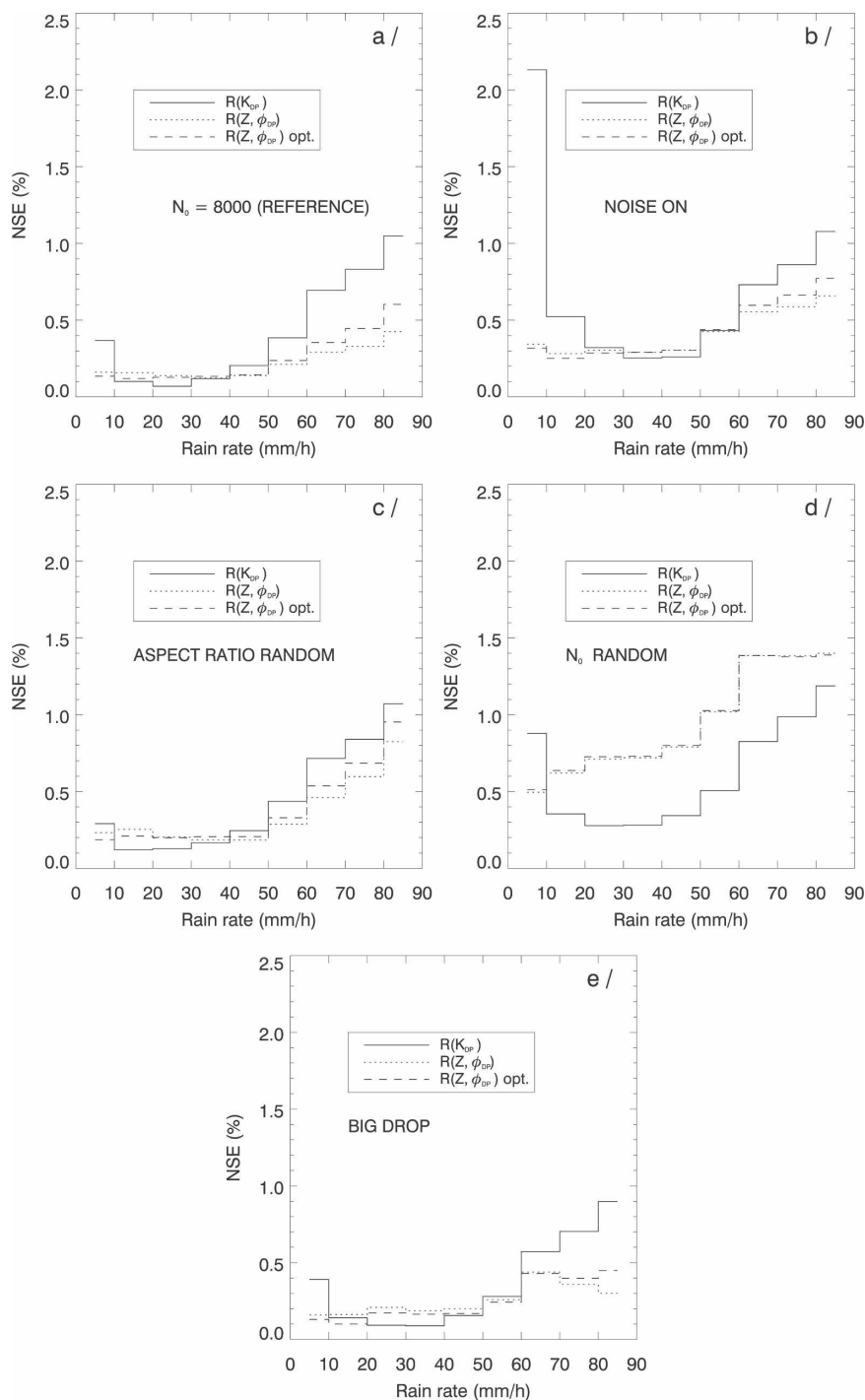
FIG. 14. Same as Fig. 13, but showing the NB.

FIG. 15. Analysis of the NSE as a function of the rain rate. The retrieval was applied for the five options of the direct model, as indicated on the plots. For the retrieval, the coefficients are calculated over the range 0.1–50 mm h^{-1} and with the Andsager shape, except for the random aspect ratio simulation where the linear shape ($\beta = 0.062$) is used.

other coefficients of that scheme are hardly determinant.

Finally, it is interesting to analyze the scores as a function of the rain rates, and also as a function of the

PIA of the radial the estimated rainfall comes from. This is done in Figs. 15 and 16. The results are presented for the five direct model's options (reference, noise on, randomized aspect ratio, big drop, and ran-
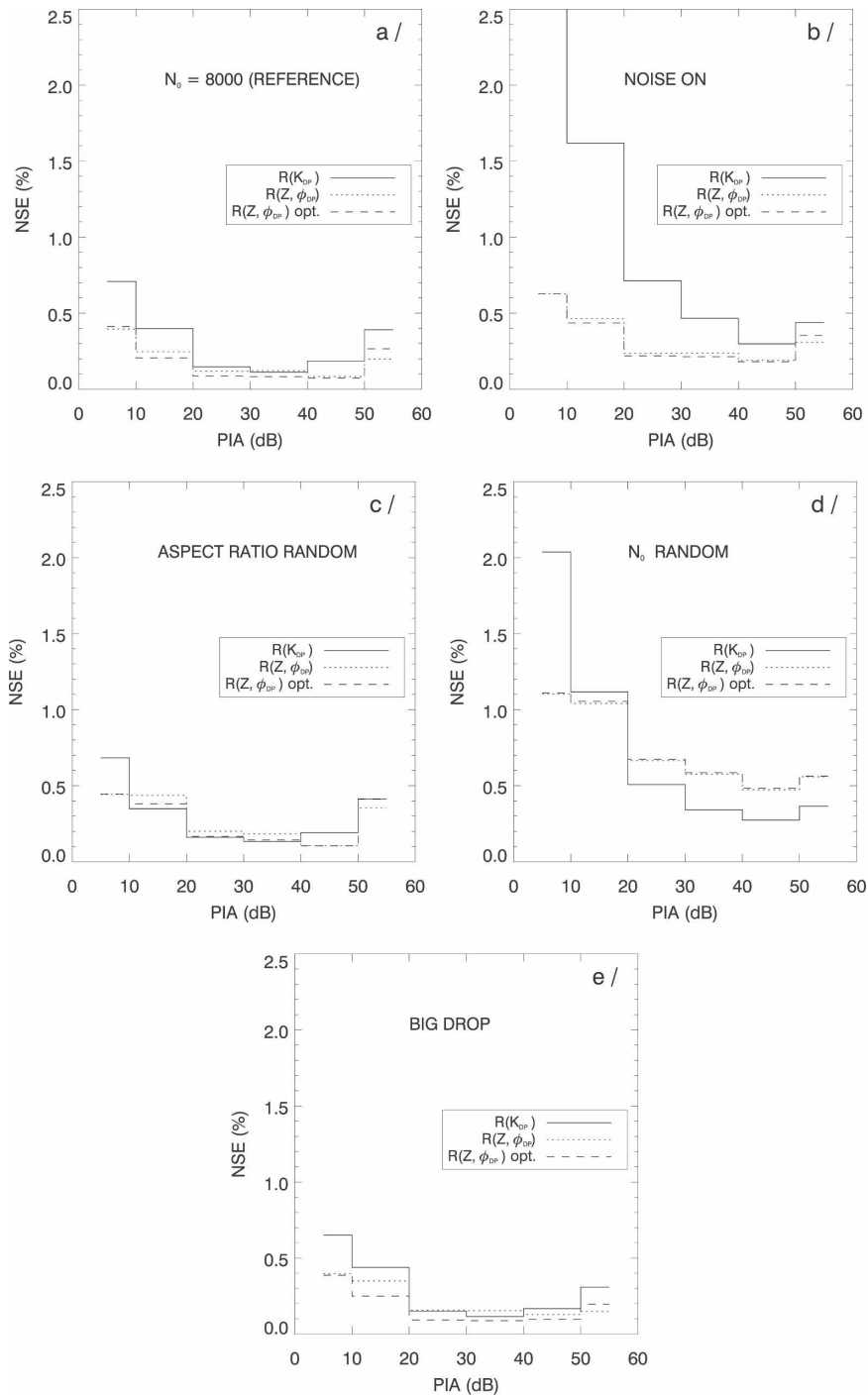
FIG. 16. Same as Fig. 15, but the NSE score is analyzed as a function of the PIA over the radial where the rain rates are estimated.

domized N_0), for the two schemes $R(K_{DP})$ and $R(Z, \phi_{DP})$ and also, for the latest, with the option $R(Z, \phi_{DP})_{opt}$. The coefficients are calculated for one oblateness law only (the "Andsager" law, except for the random oblateness simulation where the linear shape, with $\beta = 0.062$ is used) and the rain range (0.1–50 mm h^{-1}). It can be seen that both the measurement uncertainty and the gate-to-gate variability of N_0 affects the performances of R–K_{DP} for the small rain rates. In general the $R(K_{DP})$ scheme performs the best for the medium
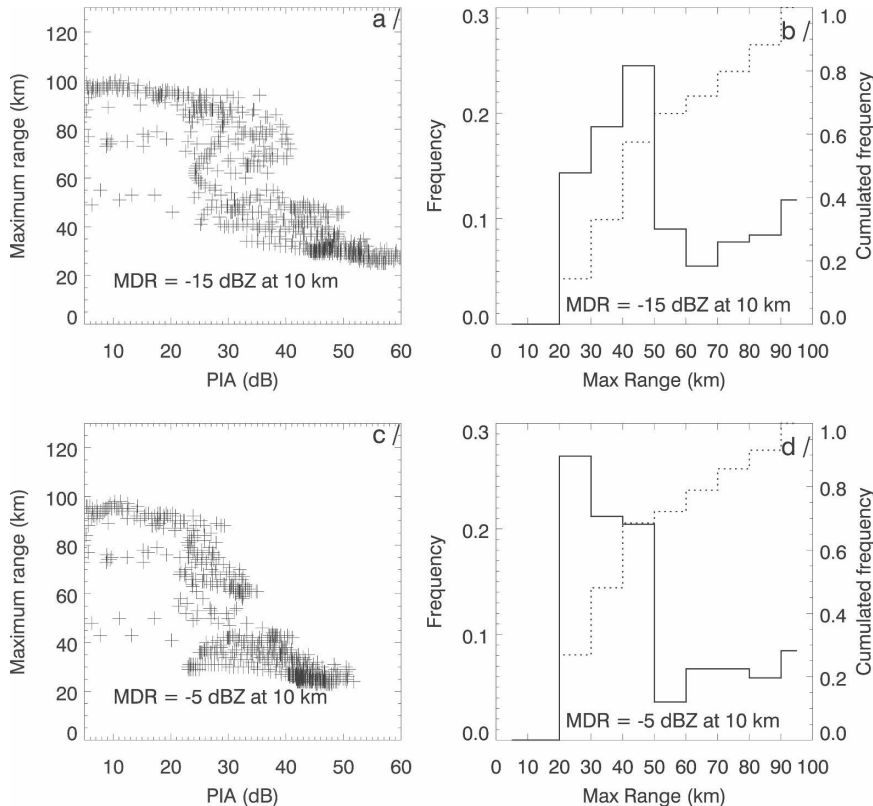
FIG. 17. Statistics on the maximum range of detection (or distance of total attenuation) for all the radials, of all the PPIs of the simulated scans. (a), (b) An MDR of −15 dBZ at 10 km and (c), (d) an MDR of −5 dBZ at 10 km. Scatterplots of the maximum range as a function of the PIA are displayed in (a) and (c). The frequency of occurrence (solid line) and the cumulative probability (dotted line) of the maximum detection range are presented in (b) and (d).

range of rain rates, while the profiler is better for both low and high rain rates. This difference of performance with rain rate is enhanced for the random N_0 simulation. Figure 16 shows that both schemes tend to perform better when the PIA increases (up to the range of 40 dB).

e. Maximum range of detection

At X band, one serious practical issue is the total attenuation of the signal in rain that leads to a reduction in the radar detection range. In the previous sections, we have used the simulator to check the quality of the rainfall estimation in the area where the estimation is possible. In Fig. 17 we illustrate the problem of total attenuation and range limitations at X band. It depends on the radar sensitivity (which we parameterized here with the minimum detectable reflectivity at range 10 km, MDR) and on the distribution of rainfall rates along the path, which controls the PIA. Recall that our simulation is representative of a tropical environment

with a high percentage of medium-to-heavy rainfalls (Fig. 8a). In these conditions we find that for our standard value of MDR (−15 dBZ at 10 km) the maximum range is greater than 40 km in 70% of cases, and its value is below 30 km in less 15% of cases. If the radar sensitivity is degraded to a MDR of −5 dBZ at 10 km, we find that the maximum range is above 40 km in 50% of cases only and below 30 km in 25% of cases, but never below 20 km. The objective of our own radar experiment is the monitoring of a small, 600 km², catchment. For such an application, we find that even the radar with the lowest sensitivity is acceptable. Such statistics need to be backed up with real observations, as the ones that are currently carried out in Africa with the Xport radar.

5. Conclusions

A radar simulator has been developed to test rainfall retrieval schemes, in preparation of the installation of

an X-band polarimetric radar in northern Benin as part of the international African Monsoon Multidisciplinary Analysis (AMMA) project. The simulator is applicable to the output fields of a numerical mesoscale model. It uses as input the mixing ratios of hydrometeors provided by the model and extracted on a polar grid using an appropriate interpolation scheme. Compared to other simulators developed previously, this one offers the following advantages:

- It is modular, so various aspects of the radar measurement and several sources of uncertainty in the retrieval algorithms can be analyzed independently.
- The radar polarimetric variables are calculated using a T-matrix code. Both backscattering and propagation effects are taken into account to calculate the reflectivities in both channels and the differential phase shift.
- The natural variability of drop size distributions is taken into account at each gate by setting several parameters of the drop size distribution, namely the intercept parameter N_0, the minimum and maximum diameters of the drops, and the shape parameter μ of the normalized gamma distribution.
- Using the water contents extracted from a mesoscale model offers more realism than simple mathematical models. At the same time, keeping the simulator external (off line) allows more flexibility.

The radar we installed in Benin (Xport) operates in the X band, and we focus on these frequencies. With this setup, we revisited in a systematic way the sensitivity of the backscattering (Z_H, Z_{DR}) and propagation (A_H, K_{DP}, or the integral ϕ_{DP}) variables to the natural variability of rain: temperature, shapes of drops, shape, and width of the drop size distribution (DSD). We also analyzed the variability of the power-law relationships between pairs of radar variables and also between a given radar variable and the rain rate. This led us to restrict our tests to two schemes in which the estimation of rain rate is based on the propagation parameters (K_{DP} or A_H) rather than on the backscattering variables (Z_{DR}, Z). The first scheme is a simple R–K_{DP} relationship, and the second one is a profiler that estimates A_H using both the path-integrated ϕ_{DP} and the reflectivity (as in Testud et al. 2000 or Anagnostou et al. 2004). The derivation of the coefficients used in these two algorithms raised two issues that were poorly discussed previously:

1) Because the relationships between radar variables and rain are not perfect power laws (especially at X-band where the Rayleigh assumption breaks down) the calculation of these coefficients by linear fit (in

log scale) is very sensitive to the range of rain rates considered for the fit.

2) Concerning the profiling $R(Z, \phi_{DP})$ scheme, we found that the relationship between the specific attenuation and K_{DP} is dependent on many factors (temperature, shapes of drops, shape and width of the DSD). When applying the scheme we calculate the path-integrated attenuation (PIA) from ϕ_{DP} over long rather than short ranges, so that the variability averages out. We also found that the natural variability of the coefficient a_{A-Z}, between specific attenuation and reflectivity is high and cannot be interpreted only as a variation of the intercept parameter N_0.

In the next step we proceeded to evaluate the scores of the two selected rain estimators for the type of rainfall we expect in Benin. For this purpose the simulator was used with a case study of an African squall line generated by the Meso-NH model. We analyzed the relative sensitivity of the two estimators to several aspects of rain variability and to measurement uncertainties. We found that

1) The uncertainty in the oblateness law affects the R–K_{DP} scheme less than the profiler $R(Z, \phi_{DP})$ scheme. The latter scheme is improved if the A_H–K_{DP} relationship is initially adjusted using values of the PIA and ϕ_{DP}.

2) For the two schemes, the random variability of N_0 around its mean is a very important source of error, as is to a lesser extent the gate-to-gate variability of the mean oblateness. These two examples of natural variability are shown to have an effect equivalent to or stronger than standard measurement uncertainties.

When we analyzed the scores as a function of the rainfall rates, we found that R–K_{DP} performs better for rain rates between 10 and 40 mm h^{-1}, while the profiler performs better for the lowest and the highest rain rates of our distribution.

This work opens new areas of investigation. First, the sensitivity analysis presented here is limited to two algorithms and we plan to extend the work to self-tuning algorithms that compensate for drop shape variability (such as the ones by Matrosov et al. 2005; Park et al. 2005a,b; Anagnostou et al. 2004). We could extend the analysis to rain accumulations and not just rain rates. We could also investigate other types of precipitation and the application to hydrometeor sorting. X-band polarimetric measurements are currently being gathered in Benin, West Africa, and the data will be interpreted in light of the present work.

REFERENCES

Anagnostou, E. N., M. N. Anagnostou, W. F. Krajewski, A. Kruger, and B. Miriovsky, 2004: High-resolution rainfall estimation from X-band polarimetric radar measurements. *J. Hydrometeor.,* **5,** 110–128.

Andsager, K., K. V. Beard, and N. F. Laird, 1999: Laboratory measurements on axis ratios for large raindrops. *J. Atmos. Sci.,* **56,** 2673–2683.

Berne, A., and R. Uijlenhoet, 2005: A stochastic model of range profiles of raindrop size distributions: Application to radar attenuation correction. *Geophys. Res. Lett.,* **32,** L10803, doi:10.1029/2004GL021899.

Brandes, E. A., A. V. Ryzhkov, and D. S. Zrnić, 2001: An evaluation of radar rainfall estimates from specific differential phase. *J. Atmos. Oceanic Technol.,* **18,** 363–375.

Bringi, V. N., and V. Chandrasekar, 2001: *Polarimetric Doppler Weather Radar: Principles and Applications.* Cambridge University Press, 636 pp.

——, ——, N. Balakrishnan, and D. S. Zrnić, 1990: An examination of propagation effects in rainfall on radar measurements at microwave frequencies. *J. Atmos. Oceanic Technol.,* **7,** 829–840.

Carey, L. D., S. A. Rutledge, D. A. Ahijevych, and T. D. Keenan, 2000: Correcting propagation effects in C-band polarimetric radar observations of tropical convection using differential propagation phase. *J. Appl. Meteor.,* **39,** 1405–1433.

Caumont, O., and Coauthors, 2005: A radar observation operator for high-resolution nonhydrostatic numerical weather prediction. *J. Atmos. Oceanic Technol.,* **22,** 1405–1433.

Cazenave, F., M. Gosset, and J. Dossougoin, 2006: Xport, a compact radar for hydrological application. *Proc. Fourth European Conf. on Radar in Meteorology and Hydrology (ERAD 2006),* Barcelona, Spain, Copernicus Group, P2.4. [Available online at http://www.grahi.upc.es/ERAD2006/proceedingsMask/00027.pdf.]

Delrieu, G., S. Caoudal, and J. D. Creutin, 1997: Feasability of using mountain return for the correction of ground-based X-band weather radar data. *J. Atmos. Oceanic Technol.,* **14,** 368–385.

Diongue, A., J.-P. Lafore, J.-L. Redelsperger, and R. Roca, 2002: Numerical study of a Sahelian synoptic weather system: Initiation and mature stages of convection and its interactions with the large-scale dynamics. *Quart. J. Roy. Meteor. Soc.,* **128,** 1899–1927.

Fabry, F., G. Austin, and D. Tees, 1992: The accuracy of rainfall estimates by radar as a function of range. *Quart. J. Roy. Meteor. Soc.,* **118,** 435–453.

Goddard, J. W. F., K. L. Morgan, A. J. Illingworth, and H. Sauvageot, 1995: Dual wavelength polarization measurements in precipitation using the CAMRA and Rabelais radars. Preprints, *27th Conf. on Radar Meteorology,* Vail, CO, Amer. Meteor. Soc., 196–198.

Gorgucci, E., G. Scarchilli, V. Chandrasekar, and V. N. Bringi, 2000: Measurement of mean raindrop shape from polarimetric radar observations. *J. Atmos. Sci.,* **57,** 3406–3413.

——, ——, ——, and ——, 2001: Rainfall estimation from polarimetric radar measurements: Composite algorithms immune to variability in raindrop shape–size relation. *J. Atmos. Oceanic Technol.,* **18,** 1773–1786.

Gosset, M., 2004: Effect of nonuniform beam filling on the propagation of radar signals at X-band frequencies. Part II: Exami-

nation of differential phase shift. *J. Atmos. Oceanic Technol.,* **21,** 358–367.

——, and I. Zawadzki, 2001: Effect of nonuniform beam filling on the propagation of the radar signal at X-band frequencies. Part I: Changes in the *k(Z)* relationship. *J. Atmos. Oceanic Technol.,* **18,** 1113–1126.

Goutorbe, J.-P., and Coauthors, 1994: HAPEX-Sahel: A large-scale study of land–atmosphere interactions in the semi-arid tropics. *Ann. Geophys.,* **12,** 53–64.

Haase, G., and S. Crewell, 2000: Simulation of radar reflectivities using a mesoscale weather forecast model. *Water Resour. Res.,* **38,** 2221–2231.

Hitschfeld, W., and J. Bordan, 1954: Errors inherent in the radar measurement of rainfall at attenuating wavelengths. *J. Meteor.,* **11,** 58–67.

Illingworth, A. J., and T. M. Blackman, 2002: The need to represent raindrop size spectra as normalized gamma distributions for interpretation of polarization radar observations. *J. Appl. Meteor.,* **41,** 286–297.

Lafore, J. P., and Coauthors, 1998: The Meso-NH Atmospheric Simulation System. Part I: Adiabatic formulation and control simulations. *Ann. Geophys.,* **16,** 90–108.

Marzoug, M., and P. Amayenc, 1991: Improved range-profiling algorithm of rainfall rate from a spaceborne radar with path-integrated attenuation constraint. *IEEE Trans. Geosci. Remote Sens.,* **29,** 584–592.

Matrosov, S. Y., R. A. Kropfli, R. F. Reinking, and B. E. Martner, 1999: Prospects for measuring rainfall using propagation differential phase in X- and K_a-radar bands. *J. Appl. Meteor.,* **38,** 766–776.

——, K. A. Clark, B. E. Martner, and A. Tokay, 2002: X-band polarimetric radar measurements of rainfall. *J. Appl. Meteor.,* **41,** 941–952.

——, D. E. Kingsmill, B. E. Martner, and F. M. Ralph, 2005: The utility of X-band polarimetric radar for quantitative estimates of rainfall parameters. *J. Hydrometeor.,* **6,** 248–262.

Miriovsky, B. J., and Coauthors, 2004: An experimental study of small-scale variability of radar reflectivity using disdrometer observations. *J. Appl. Meteor.,* **43,** 106–118.

Mishchenko, M. I., and L. D. Travis, 1998: Capabilities and limitations of a current FORTRAN implementation of the T-matrix method for randomly oriented, rotationally symmetric scatterers. *J. Quant. Spectrosc. Radiat. Transfer,* **60,** 309–324.

Park, S.-G., V. N. Bringi, V. Chandrasekar, M. Maki, and K. Iwanami, 2005a: Correction of radar reflectivity and differential reflectivity for rain attenuation at X band. Part I: Theoretical and empirical basis. *J. Atmos. Oceanic Technol.,* **22,** 1621–1632.

——, M. Maki, K. Iwanami, V. N. Bringi, and V. Chandrasekar, 2005b: Correction of radar reflectivity and differential reflectivity for rain attenuation at X band. Part II: Evaluation and application. *J. Atmos. Oceanic Technol.,* **22,** 1633–1655.

Pellarin, T., G. Delrieu, G.-M. Saulnier, H. Andrieu, B. Vignal, and J.-D. Creutin, 2002: Hydrologic visibility of weather radar systems operating in mountainous regions: Case study for the Ardèche catchment (France). *J. Hydrometeor.,* **3,** 539–555.

Rahimi, A. R., A. R. Holt, G. J. G. Upton, and R. J. Cummings, 2003: Use of dual-frequency microwave links for measuring path-averaged rainfall. *J. Geophys. Res.,* **108,** 4467, doi:10.1029/2002JD003202.

Redelsperger, J.-L., and Coauthors, 2006: AMMA, une étude

multidisciplinaire de la Mousson Ouest-Africaine. *Météorologie,* **54,** 22–32.

Ryzhkov, A. V., and D. Zrnić, 1998: Beamwidth effects on the differential phase measurements of rain. *J. Atmos. Oceanic Technol.,* **15,** 624–634.

Sachidananda, M., and D. Zrnić, 1987: Rain rate estimates from differential polarization measurements. *J. Atmos. Oceanic Technol.,* **4,** 588–598.

Sánchez-Diezma, R., I. Zawadzki, and D. Sempere-Torres, 2000: Identification of the bright band through the analysis of volumetric radar data. *J. Geophys. Res.,* **105D,** 2225–2236.

Sauvageot, H., 1996: Polarimetric radar at attenuated wavelengths as a hydrological sensor. *J. Atmos. Oceanic Technol.,* **13,** 630–637.

Smyth, T. J., and A. J. Illingworth, 1998: Correction for attenuation of radar reflectivity using polarization data. *Quart. J. Roy. Meteor. Soc.,* **124,** 2393–2415.

Testud, J., E. Le Bouar, E. Obligis, and M. Ali-Mehenni, 2000: The rain profiling algorithm applied to polarimetric weather radar. *J. Atmos. Oceanic Technol.,* **17,** 332–356.

——, S. Oury, R. A. Black, P. Amayenc, and X. Dou, 2001: The concept of normalized distribution to describe raindrop spectra: A tool for cloud physics and cloud remote sensing. *J. Appl. Meteor.,* **40,** 1118–1140.

Uijlenhoet, R., M. Steiner, and J. A. Smith, 2003: Variability of raindrop size distributions in a squall line and implications for radar rainfall estimation. *J. Hydrometeor.,* **4,** 43–61.

Waldvogel, A., 1974: The N_0 jump of raindrop spectra. *J. Atmos. Sci.,* **31,** 1067–1078.

Wu, B., J. Verlinde, and J. Sun, 2000: Dynamical and microphysical retrievals from Doppler radar observations of a deep convective cloud. *J. Atmos. Sci.,* **57,** 262–283.

Xiao, Q., Y.-H. Kuo, J. Sun, W.-C. Lee, D. M. Barker, and E. Lim, 2004: Assimilation of Doppler radar observations and its impacts on forecasting of the landfalling typhoon Rusa (2002). *Proc. Third European Conf. on Radar in Meteorology and Hydrology (ERAD3),* Visby, Sweden, European Geosciences Union, 178–182.

Zahiri, E.-P., 2007: Cycle de l'eau des systemes convectifs ouest-africain: Preparation à l'exploitation des mesures radar Xport dans AMMA par simulations. Ph.D. dissertation, Université Paul Sabatier, 256 pp.

Zawadzki, I., 1984: Factors affecting the precision of radar measurements of rain. Preprints, *22nd Conf. on Radar Meteorology,* Zurich, Switzerland, Amer. Meteor. Soc., 251–256.

Zrnić, D. S., T. D. Keenan, L. D. Carey, and P. May, 2000: Sensitivity analysis of polarimetric variables at a 5-cm wavelength in rain. *J. Appl. Meteor.,* **39,** 1514–1526.